What is the Role of Relative Humidity on Conductivity in Polymer Electrolytes?

Nico Marioni,[†] Akhila Rajesh,[†] Rahul Sujanani,[‡] Zidan Zhang,[†] Leo W. Gordon,[¶] Raphaële J. Clément,[¶] Rachel A. Segalman,[¶,‡] Benny D. Freeman,[†] and Venkat Ganesan[*,†]

[†]*McKetta Department of Chemical Engineering, The University of Texas at Austin, Austin, Texas 78712, United States*

[‡]*Department of Chemical Engineering, University of California Santa Barbara, Santa Barbara, California 93106, United States*

[¶]*Materials Department and Materials Research Laboratory, University of California Santa Barbara, Santa Barbara, California 93106, United States*

E-mail: venkat@che.utexas.edu

Abstract

Ion transport properties in polymer electrolytes have been widely studied under rigorously dry and highly water-swollen conditions. However, the transition between these extremes, i.e., the low hydration regime, is still poorly understood at the molecular level and relevant to applications ranging from battery electrolytes to electrophoretic separations. In this study, we apply atomistic molecular dynamics simulations to probe the role of hydration on ion mobilities and conductivities in LiTFSI-doped polyethers at low water content (less than 10% water by volume), which corresponds to 0-80% relative humidity conditions. With increasing water content, Li^+ ions exhibit two distinct regimes in their mobilities. At low water content, the majority of the Li^+ ions are weakly hydrated (two or fewer water molecules per Li$^+$ ion), maintaining strong interactions with their polymer solvation cage, and therefore exhibit only a weak increase in mobility relative to dry conditions. As water content increases, Li$^+$ ions form complete hydration shells, residing within water-rich domains that promote faster mobilities. Further, Li$^+$ mobilities increase more significantly in polymer electrolytes composed of more hydrophilic polymers and higher salt concentrations due to the formation of larger water-rich domains. In contrast, TFSI$^-$ has comparatively weak interactions with both the polymer and water, exhibiting a monotonic increase in mobility as a function of water content. Overall, these results help clarify the molecular mechanisms underlying ionic mobilities and conductivities in polymer electrolytes at low water content.

Ion transport in dry polymer electrolytes has been widely studied due to its importance to energy applications.[1–4] In such cases, ion transport in rubbery polymer electrolytes is strongly influenced by ion-polymer solvation interactions and polymer segmental dynamics.[5–8] Ion transport in water-swollen polymer networks, generally at high water content (greater than 40% water by volume), is also a critical element of the design of both fuel cell and electrophoretic water purification systems.[9–11] In such cases, due to strong ion-water solvation interactions, ion transport is generally understood to occur via vehicular transport of ion-water complexes through water-rich domains.[12,13] Hence, diffusion within highly hydrated polymer membranes is often correlated with the aqueous solution ion diffusion coefficient scaled by a tortuosity factor that is governed by the water content in the polymer domain.[14–16] While the extreme cases of dry and highly-swollen polymer electrolytes have been studied extensively, there remain fundamental knowledge gaps in our understanding of ion transport in polymer electrolytes under low hydration conditions. More specifically, it is not well understood how ion transport transitions from being constrained by polymer segmental dynamics (ion-polymer interactions dominate) in the dry condition to vehicular ion-water transport (ion-water interactions dominate) in highly hydrated systems.

Recently,[17] we combined pulsed field gradient (PFG) NMR diffusivity measurements and equilibrium atomistic molecular dynamics (MD) simulations to probe ion and water self-diffusion in salt-doped polymer electrolytes in the transition from dry to water-swollen conditions up to 0.9 g water/g salt-doped polymer (up to 53% water by volume). Ion transport was broadly divided into two distinct regimes with respect to hydration: non-percolated and water-percolated polymer systems. The percolated regime was generally well-described by the models of hindered-transport in tortuous membranes.[14,15] However, the non-percolated regime was characterized by a complex interplay between ion-ion, ion-polymer, and ion-water solvation interactions. Notably, while ion diffusion was strongly correlated with polymer segmental dynamics under dry conditions, the addition of even small quantities of water (0.02 g water/g salt-doped polymer) significantly decreased ion-polymer interactions, and reduced the influence of polymer segmental motion on ion diffusion.

While our previous study[17] shed light on the mechanisms underpinning ion and water transport, our results were specific to equilibrium self-diffusion coefficients of the anions and cations, and pertained to moderate-to-high water content. However, there is significant interest in understanding the impact of water on *ionic conductivity* in energy storage applications.[18–20] For example, solid polymer electrolytes (SPEs) containing small quantities of water (up to 0.14 g water/g salt-doped polymer) exhibit high ionic conductivities and improved safety compared to dry SPEs, and improved electrochemical stability compared to water-in-salt electrolytes.[21] Further understanding of such materials offers critical insights into the development of safe, highly conductive aqueous battery systems as an alternative to traditional lithium-ion batteries.[22] Similarly, ionic conductivities of SPEs exposed to humidity increase by several orders of magnitude depending on the salt and polymer material.[23–26] The mechanisms underlying such results are still not fully clarified.

In a recent study,[27] our experimental team measured ionic conductivity in lithium bis(trifluoromethane)sulfonimide (LiTFSI)-doped polyethers under controlled humidity conditions (0-80% relative humidity), probing water uptake and ionic conductivity in the *non-percolated regime* up to 0.07 g water/g salt-doped polymer (corresponding to less than 10% water by volume). In contrast to previous literature,[23–26] ionic conductivity is observed to increase by only a factor of 2-4 going from dry to 80% relative humidity conditions, further highlighting the importance of studying this regime. More specifically, ionic conductivity increased non-linearly as a function of water uptake, with a weaker increase at low water content followed by a significantly stronger increase at higher water content (still within the non-percolated regime). Interestingly, at low water content, the normalized molar conductivity values of different polyether electrolytes were generally correlated with the water content expressed as the number of water molecules per Li^+ ion, $N_{\mathrm{H_2O}}/N_{\mathrm{Li}^+}$. However, the molar conductivities deviated from such a correlation once $N_{\mathrm{H_2O}}/N_{\mathrm{Li}^+}$ exceeded the hydration number of Li^+ ions in bulk aqueous solution (i.e., $N_{\mathrm{H_2O}}/N_{\mathrm{Li}^+} = 4$).[28] Further, we presented PFG NMR diffusivities of Li^+ and TFSI^-, and argued that much of the observed conductivity increase arose from the influence of water on Li^+ ion mobilities rather than increased polymer segmental dynamics due to plasticization by water (decreased glass transition temperature).

This study is motivated by the above experimental results, and uses computer simulations to understand in detail the underlying mechanisms of conductivity and mobilities in salt-doped polymer electrolytes at low water contents. We note that conductivity may be broken down into the individual ionic contributions as:[29]

$$\Lambda_{\mathrm{m}} = F \sum_i z_i \mu_i, \tag{1}$$

where Λ_{m} is the concentration-normalized (molar) conductivity, F is Faraday's constant, and z_i and μ_i are the ionic charge and ionic mobility of species i, respectively. While our earlier study focused on the mechanisms underlying self-diffusion coefficients at high water content,[17] there is little known about the role of hydration on ionic mobilities and conductivities, especially at low water content. Indeed, ion self-diffusion coefficients do not account for ionic correlations arising from ion pairing, which can lead to deviations of ionic mobilities and conductivity from the ideal Nernst-Einstein values, especially in concentrated battery electrolytes.[29–33] In contrast, atomistic MD simulations can systematically probe the impact of water content, polymer identity, and salt concentration on ionic mobilities. Specifically, non-equilibrium electric field-driven MD simulations permit the direct measurement of ionic mobilities[29,31] and can identify the relative roles of Li^+ and $TFSI^-$ dynamics in influencing the conductivity. Furthermore, simultaneous characterization of structural features can provide mechanistic insights on the role of ion-polymer, ion-water, and ion-ion interactions in modulating ion mobilities and correlations. Using such tools, we seek to understand the role of hydration on the mobilities of Li^+ and $TFSI^-$ ions and the origins underlying the two regime behavior noted in experiments.[27] Of further interest are the influences of salt concentration and polymer chemistries on ion conduction, which were explored preliminarily in our experimental study.[27]

In the present study, we performed equilibrium and non-equilibrium atomistic MD simulations of linear poly(ethylene oxide)-poly(allyl glycidyl ether) (PEO-PAGE) statistical polymers of varying composition, where the addition of AGE monomer to PEO reduces the hydrophilicity of the polymer matrix and enables tuning of the water uptake.[27] The polymers were doped with LiTFSI at two different salt loadings and with water uptake values comparable to the experimental systems probed by Sujanani et al.[27] Specifically, we performed simulations of 10-mer polymer chains with a 100:0 (PEO), 70:30 (PEO-PAGE), and 0:100 (PAGE) EO:AGE molar ratio containing $r = 0.045$ or 0.10 LiTFSI salt pairs per polymer repeat unit. Although PEO was not experimentally studied by Sujanani et al.[27] due to high crystallinity at room temperature ($T_c \simeq 323$ K at $r = 0.045$, where T_c is the crystallization temperature[34]), simulations do not suffer from such crystalline behavior at the temperatures simulated ($T = 400$ K, see simulation details below) and provide a framework to investigate the interplay between ion-polymer, ion-water and ion-ion interactions.

For brevity, the majority of the simulation details are presented in Section S1 of the Supporting Information. To model bulk SPE systems equilibrated under 0-80% relative humidity conditions, each dry polymer system was initialized with a range of water contents spanning from 0 to 6 water molecules per $\mathrm{Li^+}$ ion (See Table S6). The all-atom optimized potentials for liquid simulations (OPLS-AA),[35,36] Madrid,[37] OPLS-2009IL,[38,39] and TIP4P-2005[40] force field parameterizations were chosen to model the polymer, $\mathrm{Li^+}$, $\mathrm{TFSI^-}$, and water, respectively. As in previous work,[17] a multi-step equilibration procedure is used to obtain an equilibrated state followed by a 200 ns NVT production run for data collection. To probe ionic mobilities,[29,31] following the production run, non-equilibrium simulations were performed by applying an electric field to the simulation box for 50 ns under NVT conditions. By measuring a range of field strengths, $E = 0.02 - 0.10$ V/nm, the linear response regime was probed to extract the zero-field ionic mobilities as a function of water content (See Sections S1.2 and S2.1 for more details). Unlike conductivities, individual ion mobilities are reference frame dependent. Herein, ionic mobilities are presented relative to the polymer-fixed reference frame. While there is some debate on appropriate reference frames for comparison to experiments,[41,42] in Section S3, we show that the following analysis is qualitatively preserved in other frames of reference. All simulations were performed at a temperature of 400 K with relatively short polymer chains (10-mers) to ensure fast dynamics to obtain sufficient statistical significance for ionic mobilities. While this is a higher temperature and lower polymer molecular weight compared to experiments, the underlying physics (in amorphous materials) are not expected to change significantly as a function of temperature or molecular weight (Section S2.1.1 compares our simulation results to the experimental results presented by Sujanani et al.[27]).[17] Through such a framework, we probe the impact of ion-water and ion-polymer solvation interactions on the mechanisms underlying conductivity of polymer electrolytes.

Figure 1A displays the molar conductivities, Λ_m, normalized by their value under dry conditions, $\Lambda_\mathrm{m}^\mathrm{Dry}$ (unnormalized Λ_m results are displayed in Figure S3A), as a function of the ratio of the number of water molecules, $N_{\mathrm{H_2O}}$, to the number of $\mathrm{Li^+}$ ions, $N_{\mathrm{Li^+}}$, in the system. The overall conductivity is found to increase with water content, albeit to varying extents depending on the salt concentration and polymer chemistry. Specifically, systems at higher salt loadings, $r = 0.10$, exhibit a more significant increase in conductivity compared to systems at lower salt loadings, $r = 0.045$. At low water content, PAGE systems exhibit a larger increase in conductivity relative to the dry condition than PEO-PAGE and PEO systems. However, both PEO-PAGE and PEO systems exhibit a more significant increase in conductivity relative to PAGE with increasing water content.

To better understand the connection between Li^+ hydration and ionic conductivity, Figures 1B and C display the $TFSI^-$ and Li^+ mobilities (normalized to their respective values under dry conditions) as a function of N_{H_2O}/N_{Li^+}, respectively. $TFSI^-$ mobilities, within error, linearly increase with increasing N_{H_2O}/N_{Li^+}. In contrast, at low water contents corresponding to $N_{H_2O}/N_{Li^+} < 2$, Li^+ mobilities are almost constant within error, maintaining the same mobility as under dry conditions. As the water content increases beyond $N_{H_2O}/N_{Li^+} \simeq 2$, Li^+ mobilities increase. The latter increase relative to the dry state is more pronounced for systems at high salt loadings, $r = 0.10$, and for PEO-containing systems. We note that $TFSI^-$ mobilities are significantly larger than Li^+ mobilities (cf. unnormalized $TFSI^-$ and Li^+ mobilities in Figures S3B and C, respectively). Therefore, the conductivity trends in Figure 1A are dominated by changes in $TFSI^-$ conduction with water content.

Atomistic simulations allow us to directly probe the local solvation environment of Li^+ and $TFSI^-$ ions to unravel the mechanistic origins of the trends in the mobilities shown in Figures 1B and C (See Section S2.2 for more details on the methodology). Figures 2A and B display the (A) $TFSI^-$ and (B) Li^+ mobilities normalized to their values under dry conditions as a function of the $TFSI^- -$ and $Li^+ -$ water solvation numbers. The water solvation number, n_{i-H_2O}, is defined as the average number of water molecules in the first coordination shell of an ion of species i . We note that $n_{Li^+-H_2O}$ is distinct from N_{H_2O}/N_{Li^+} in that $n_{Li^+-H_2O}$ only considers water molecules that specifically solvate the Li^+ ions, rather than a simple ratio of the number of water molecules and Li^+ ions in the system. In this representation, the $TFSI^-$ mobilities of all systems exhibit a universal correlation to $n_{TFSI^--H_2O}$. In contrast, Li^+ mobilities are constant for all systems and display a similar correlation for

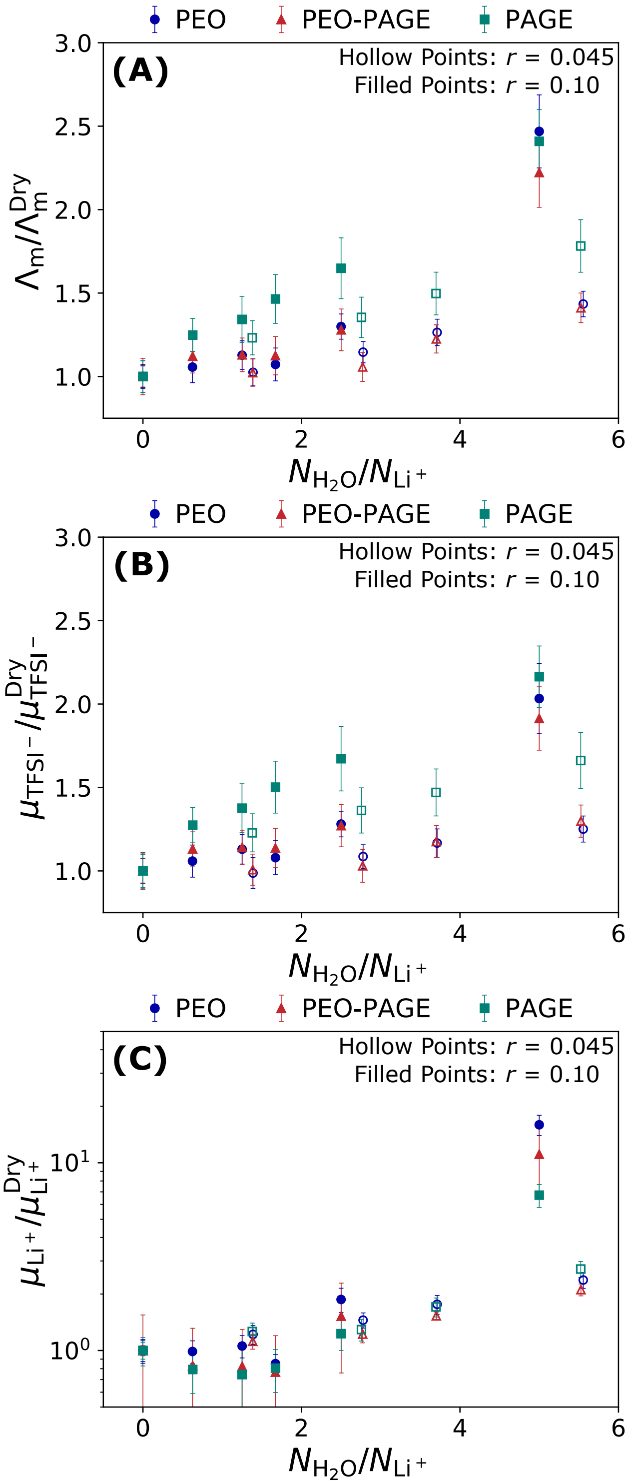

Figure 1: Ratio of the (A) molar conductivity, (B) TFSI$^-$ mobility, and (C) Li$^+$ mobility to the value under dry conditions as a function of the number of water molecules per Li$^+$ ion. Hollow and filled points represent systems at lower (r = 0.045) and higher (r = 0.10) salt loadings, respectively.

$n_{\mathrm{Li^+-H_2O}} < 2$. However, Li$^+$ mobilities increase significantly when $n_{\mathrm{Li^+-H_2O}} > 2$, and a more significant increase is noted at higher salt loading and for PEO-containing systems (PEO > PEO-PAGE > PAGE).

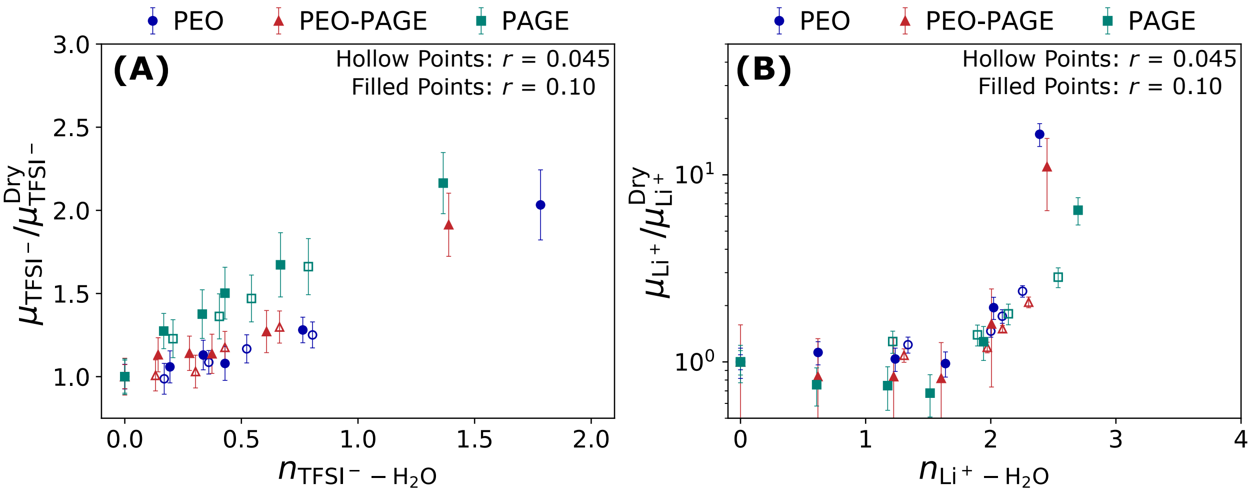

Figure 2: Ratio of the (A) TFSI$^-$ and (B) Li$^+$ mobilities to the value under dry conditions as a function of the TFSI$^-$ $-$ H$_2$O and Li$^+$ $-$ H$_2$O solvation numbers, respectively. Hollow and filled points represent systems at lower ($r = 0.045$) and higher ($r = 0.10$) salt loadings, respectively.

We attribute the difference noted above in the trends in the Li$^+$ and TFSI$^-$ mobilities to the different interactions between the respective ions and polymer and water. As we discuss in Section S2.2, the delocalized charge on the TFSI$^-$ anion leads to only weak solvation by both the polymer and water. Therefore, we may expect TFSI$^-$ ions to be less impacted by the specific solvation environment than Li$^+$ ions. Hence, the increase in the TFSI$^-$ mobility with increasing water content can be understood to be related to the increase in local dynamics (i.e., lower viscosity) around TFSI$^-$ ions as the local environment is filled with water molecules instead of slow polymer segments. When it comes to Li$^+$ ions in dry polymer electrolytes, Li$^+$ ions coordinate strongly with ether oxygen atoms and their diffusion behavior is governed by polymer segmental motions. In contrast, in aqueous solutions, Li$^+$ ions diffuse as long-lived Li$^+$-water complexes. From these contrasting mechanisms, the trends in Li$^+$ mobility as a function of water content likely arise from the transition from slow, "condensed" Li$^+$ ions solvated by an ether oxygen solvation cage to fast, "free" Li$^+$

ions that are fully solvated by water molecules.

To probe this hypothesis regarding Li^+ ion mobilities, Figure 3A displays the fraction of "free" Li^+ ions as a function of the Li^+-water solvation number. Here, "free" Li^+ ions refer to ions that are not solvated by polymer ether oxygen atoms. Interestingly, we observe two distinct regimes, which is consistent with our previous analysis: at low water contents (i.e., $n_{\mathrm{Li}^+-\mathrm{H_2O}} < 2$), all Li^+ ions are condensed within the polymer chains. However, for $n_{\mathrm{Li}^+-\mathrm{H_2O}} > 2$, we observe a significant increase in the fraction of free Li^+ ions (See Section S2.2 and Figures S7-S9 for more discussion on Li^+ solvation and the role of polymer chemistry). Taken together, polyether chains form a solvation cage around Li^+ ions under dry conditions. As water molecules enter the system, they solvate Li^+ ions up to a coordination of two water molecules per Li^+ ion on average. However, Li^+ ions remain condensed with the polymer chains, maintaining a mobility comparable to dry conditions (Figure 2A, $n_{\mathrm{Li}^+-\mathrm{H_2O}} < 2$). Upon further hydration, some Li^+ ions disassociate from the polymer chains, forming "free" Li^+ ions solvated by water molecules leading to a drastic increase in ion conduction compared to dry conditions (Figure 2A, $n_{\mathrm{Li}^+-\mathrm{H_2O}} > 2$).

Comparing the results presented in Figures 2B and 3A, it becomes clear that the dependence of the Li^+ mobility on the salt concentration and polymer chemistry cannot be explained by the fraction of "free" Li^+ ions alone (shown in Figure 3B, which displays the normalized Li^+ mobilities as a function of the "free" ion fraction). The Li^+ mobility is likely additionally influenced by the size of (non-percolating) water clusters in the respective systems. Indeed, larger water clusters can be expected to facilitate faster "free" Li^+ ion transport since the dynamics in such water-rich domains can be expected to approach bulk-like characteristics. Figure 3C displays the average number of water molecules within a continuous water cluster as a function of the Li^+-water solvation number, where a water cluster is defined as a group of water molecules with overlapping water-water coordination shells (See Section S2.3 for more details on the methodology). At low water content, the average cluster contains one or two water molecules, and there is little difference between

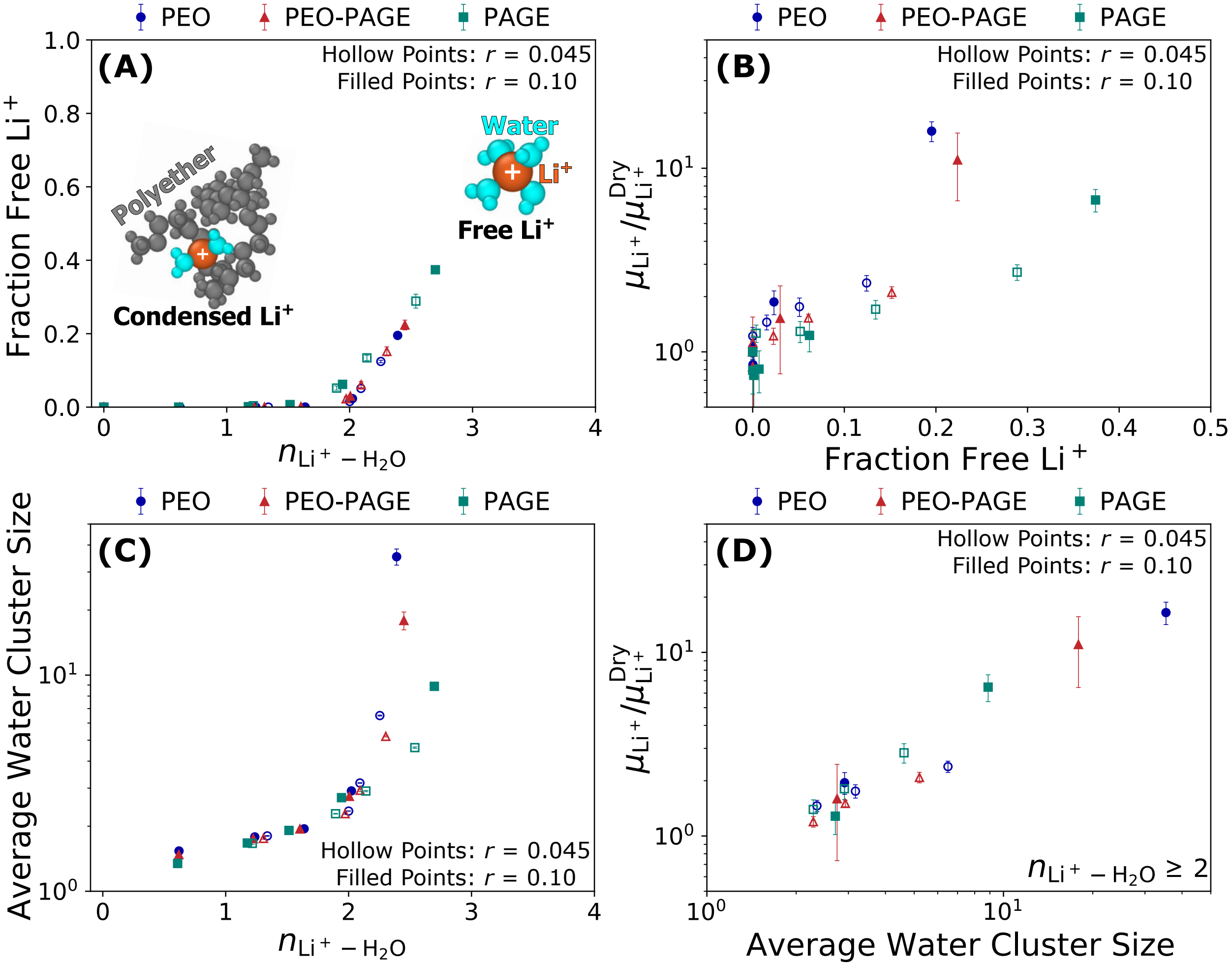

Figure 3: (A) Fraction of "free" Li$^+$ ions as a function of the $Li^+ - H_2O$ solvation number, where "free" Li$^+$ ions are not solvated by polymer ether oxygen atoms. (B) Ratio of the Li$^+$ mobility to the value under dry conditions as a function of the fraction of "free" Li$^+$ ions. (C) Average water cluster size as a function of the $Li^+ - H_2O$ solvation number. (D) Ratio of the Li$^+$ mobility to its value under dry conditions as a function of the average water cluster size. Data is limited to systems that contain "free" Li$^+$ ions. (A-D) Hollow and filled points represent systems at lower ($r = 0.045$) and higher ($r = 0.10$) salt loadings, respectively.

polymer chemistries. We attribute this result to the preferential solvation of Li^+ ions up to $n_{\mathrm{Li}^+-\mathrm{H}_2\mathrm{O}} = 2$. As water content increases, favorable water-water interactions lead to the formation of larger water clusters, where polymer chemistries with higher EO and salt contents exhibit larger water clusters. We attribute this result to the higher water content (by volume) of PEO systems compared to PAGE due to the higher hydrophilicity of EO repeat units compared to AGE (See water uptake as a function of relative humidity measured by Sujanani et al.[27]), and the higher concentration of hygroscopic LiTFSI salt in PEO compared to PAGE under the salt loading conditions of this study (See water uptakes values and salt concentrations in Table S6).

The impact of water cluster size on Li^+ mobility is easier to see in Figure 3D, which displays the Li^+ mobilities normalized to their respective values under dry conditions as a function of the average water cluster size. For clarity, we only display the data points for systems that contain "free" Li^+ ions, i.e., $n_{\mathrm{Li}^+-\mathrm{H}_2\mathrm{O}} > 2$. We observe a reasonable correlation between Li^+ mobility and water cluster size across all systems studied, suggesting that both "free" Li^+ ions and large water cluster domains are necessary to facilitate fast Li^+ conduction.

Interestingly, systems with larger water clusters, i.e., PEO, also tend to have less "free" Li^+ ions compared to PAGE systems with smaller water clusters (cf. Figures 3A and B). As discussed in Section S2.2, such a trade-off is driven by the ratio of the $\mathrm{Li}^+ - \mathrm{H}_2\mathrm{O}$ to $\mathrm{Li}^+ - \mathrm{EO}$ free energies of solvation (cf. Figures S7A and B), where it is more energetically favorable for Li^+ ions to be solvated by water molecules over polymer ether oxygen atoms in PAGE systems compared to PEO systems. We rationalize such a difference by the steric hindrance of AGE side-chains which prevent favorable $\mathrm{Li}^+ - \mathrm{H}_2\mathrm{O} - \mathrm{EO}$ complexation, thereby promoting Li^+ disassociation from the polymer chains to form Li^+ ions with complete water solvation shells. Hence, there is a tradeoff in the hydrophilicity driven increase in the size of water clusters and the fraction of "free" ions.

In summary, we applied equilibrium and non-equilibrium atomistic MD simulations to probe ion conduction in LiTFSI-doped polyethers under low hydration conditions comparable to experiments[27] performed at 0-80% relative humidity. Ionic conductivity was generally correlated with the number of water molecules per Li^+ ion and exhibits a weak increase with increasing water content at low hydration conditions. We attribute this result to $TFSI^-$ conduction, which weakly increases as a function of water content due to increased local dynamics arising from water solvation. In contrast, Li^+ ions do not contribute significantly to the conductivity at low hydration due to condensation of the Li^+ ions with polymer ether oxygen solvation cages. At higher water content, conductivity increases more significantly with notable deviations based on polymer identity and salt loading. We attribute the behavior at higher water contents to enhanced Li^+ conduction due to the presence of fully hydrated, "free" Li^+ ions which reside within water clusters. The increase in Li^+ conduction is generally correlated with both the fraction of "free" Li^+ ions and the average size of water clusters, the latter of which increases with increasing polymer hydrophilicity (due to increasing EO content and salt concentration). Our findings provide a comprehensive picture of the mechanisms underlying individual ion mobilities and conductivity in polymer electrolytes at low hydration conditions.

Acknowledgement

This work was supported as part of the Center for Materials for Water and Energy Systems (M-WET), an Energy Frontier Research Center funded by the U.S. Department of Energy, Office of Science, Basic Energy Sciences, under Award #DE-SC0019272. V.G. acknowledges support from the Robert A. Welch Foundation (F-1599) to support the salary of Z.Z. who contributed to the development of non-equilibrium methodology for probing conductivities. The results in this paper were generated using high-performance computing resources provided by The University of Texas at Austin Texas Advanced Computing Center.

Supporting Information Available

The supplementary materials includes further details as follows: Section S1, details of the simulation methodology, force field parameters, and systems simulated; Section S2, methodology and supplementary results pertaining to ionic mobilities and conductivity, ion solvation, and water clustering; Section S3, supplementary results pertaining to different reference frame analyses.

References

(1) Hallinan Jr, D. T.; Balsara, N. P. Polymer electrolytes. *Annu. Rev. Mater. Sci.* **2013**, *43*, 503–525.

(2) Long, L.; Wang, S.; Xiao, M.; Meng, Y. Polymer electrolytes for lithium polymer batteries. *J. Mater. Chem. A* **2016**, *4*, 10038–10069.

(3) Arya, A.; Sharma, A. Polymer electrolytes for lithium ion batteries: a critical study. *Ionics* **2017**, *23*, 497–540.

(4) Zhou, D.; Shanmukaraj, D.; Tkacheva, A.; Armand, M.; Wang, G. Polymer electrolytes for lithium-based batteries: advances and prospects. *Chem* **2019**, *5*, 2326–2352.

(5) Borodin, O.; Smith, G. D. Mechanism of ion transport in amorphous poly(ethylene oxide)/LiTFSI from molecular dynamics simulations. *Macromolecules* **2006**, *39*, 1620–1629.

(6) Diddens, D.; Heuer, A.; Borodin, O. Understanding the lithium transport within a rouse-based model for a PEO/LiTFSI polymer electrolyte. *Macromolecules* **2010**, *43*, 2028–2036.

(7) Wang, Y.; Fan, F.; Agapov, A. L.; Saito, T.; Yang, J.; Yu, X.; Hong, K.; Mays, J.;

Sokolov, A. P. Examination of the fundamental relation between ionic transport and segmental relaxation in polymer electrolytes. *Polymer* **2014**, *55*, 4067–4076.

(8) Bocharova, V.; Sokolov, A. P. Perspectives for polymer electrolytes: a view from fundamentals of ionic conductivity. *Macromolecules* **2020**, *53*, 4141–4157.

(9) Luo, T.; Abdu, S.; Wessling, M. Selectivity of ion exchange membranes: A review. *J. Membr. Sci.* **2018**, *555*, 429–454.

(10) Sujanani, R.; Landsman, M. R.; Jiao, S.; Moon, J. D.; Shell, M. S.; Lawler, D. F.; Katz, L. E.; Freeman, B. D. Designing solute-tailored selectivity in membranes: Perspectives for water reuse and resource recovery. *ACS Macro Lett.* **2020**, *9*, 1709–1717.

(11) Nandi, A.; Rakshit, A.; Banerjee, P. *Membranes for Water Treatment and Remediation*; Springer, 2023; pp 227–248.

(12) Robinson, R. A.; Stokes, R. H. *Electrolyte Solutions*; Butterworths: London, 1965.

(13) Nightingale Jr., E. Phenomenological theory of ion solvation. Effective radii of hydrated ions. *J. Phys. Chem.* **1959**, *63*, 1381–1387.

(14) Mackie, J.; Meares, P. The diffusion of electrolytes in a cation-exchange resin membrane I. Theoretical. *Proc. R. Soc. Lond. A: Math. Phys. Eng. Sci.* **1955**, *232*, 498–509.

(15) Mackie, J.; Meares, P. The diffusion of electrolytes in a cation-exchange resin membrane. II. Experimental. *Proc. R. Soc. Lond. A: Math. Phys. Eng. Sci.* **1955**, *232*, 510–518.

(16) Zhang, H.; Geise, G. M. Modeling the water permeability and water/salt selectivity tradeoff in polymer membranes. *J. Membr. Sci.* **2016**, *520*, 790–800.

(17) Marioni, N.; Nordness, O.; Zhang, Z.; Sujanani, R.; Freeman, B. D.; Segalman, R. A.; Clément, R. J.; Ganesan, V. Ion and Water Dynamics in the Transition from Dry to Wet Conditions in Salt-Doped PEG. *ACS Macro Lett.* **2024**, *13*, 341–347.

(18) Park, J. H.; Jung, S.; Handayani, P. L.; Aluru, N.; Kim, T.; Lee, S. B.; Choi, U. H.; Lee, J. Enthalpic and entropic contributions to fast lithium ion conduction in solid-state aqueous polymer electrolytes. *J. Phys. Chem. C* **2022**, *126*, 16777–16784.

(19) Ludwig, K. B.; Correll-Brown, R.; Freidlin, M.; Garaga, M. N.; Bhattacharyya, S.; Gonzales, P. M.; Cresce, A. V.; Greenbaum, S.; Wang, C.; Kofinas, P. Examining the Electrochemical Properties of Hybrid Aqueous/Ionic Liquid Solid Polymer Electrolytes through the Lens of Composition-Function Relationships. *Adv. Energy Mater.* **2023**, *13*, 2301428.

(20) Ludwig, K. B.; Correll-Brown, R.; Freidlin, M.; Garaga, M. N.; Bhattacharyya, S.; Gonzales, P. M.; Cresce, A. V.; Greenbaum, S.; Wang, C.; Kofinas, P. Highly conductive polyacrylonitrile-based hybrid aqueous/ionic liquid solid polymer electrolytes with tunable passivation for Li-ion batteries. *Electrochim. Acta* **2023**, *453*, 142349.

(21) Widstrom, M. D.; Borodin, O.; Ludwig, K. B.; Matthews, J. E.; Bhattacharyya, S.; Garaga, M.; V. Cresce, A.; Jarry, A.; Erdi, M.; Wang, C.; Greenbaum, S.; Kofinas, P. Water domain enabled transport in polymer electrolytes for lithium-ion batteries. *Macromolecules* **2021**, *54*, 2882–2891.

(22) Ahn, H.; Kim, D.; Lee, M.; Nam, K. W. Challenges and possibilities for aqueous battery systems. *Commun. Mater.* **2023**, *4*, 37.

(23) Chandra, S.; Hashmi, S.; Prasad, G. Studies on ammonuim perchlorate doped polyethylene oxide polymer electrolyte. *Solid State Ion.* **1990**, *40*, 651–654.

(24) Lauenstein, A.; Johansson, A.; Tegenfeldt, J. Water Absorption of the Polymer Electrolyte Systems $Pb(CF_3SO_3)_2PEO_n$ and $Zn(CF_3SO_3)_2PEO_n$. *J. Electrochem. Soc.* **1994**, *141*, 1819.

(25) DeLongchamp, D. M.; Hammond, P. T. Highly ion conductive poly(ethylene oxide)-

based solid polymer electrolytes from hydrogen bonding layer-by-layer assembly. *Langmuir* **2004**, *20*, 5403–5411.

(26) Fullerton-Shirey, S. K.; Ganapatibhotla, L. V.; Shi, W.; Maranas, J. K. Influence of thermal history and humidity on the ionic conductivity of nanoparticle-filled solid polymer electrolytes. *J. Polym. Sci., Part B: Polym. Phys.* **2011**, *49*, 1496–1505.

(27) Sujanani, R.; Nguyen, P. H.; Gordon, L. W.; Bamford, J. T.; Zele, A.; Pedretti, B. J.; Lynd, N. A.; Clément, R. J.; Segalman, R. A. Influence of Water Sorption on Ionic Conductivity in Polyether Electrolytes at Low Hydration. *ACS Macro Lett.* **2024**, *14*, 64–71.

(28) Loeffler, H. H.; Rode, B. M. The hydration structure of the lithium ion. *J. Chem. Phys.* **2002**, *117*, 110–117.

(29) Zhang, Z.; Wheatle, B. K.; Krajniak, J.; Keith, J. R.; Ganesan, V. Ion Mobilities, Transference Numbers, and Inverse Haven Ratios of Polymeric Ionic Liquids. *ACS Macro Lett.* **2020**, *9*, 84–89.

(30) Nürnberg, P.; Atik, J.; Borodin, O.; Winter, M.; Paillard, E.; Schönhoff, M. Superionicity in Ionic-Liquid-Based Electrolytes Induced by Positive Ion–Ion Correlations. *J. Am. Chem. Soc.* **2022**, *144*, 4657–4666.

(31) Shen, K.-H.; Hall, L. M. Effects of ion size and dielectric constant on ion transport and transference number in polymer electrolytes. *Macromolecules* **2020**, *53*, 10086–10096.

(32) Marioni, N.; Zhang, Z.; Zofchak, E. S.; Sachar, H. S.; Kadulkar, S.; Freeman, B. D.; Ganesan, V. Impact of Ion–Ion Correlated Motion on Salt Transport in Solvated Ion Exchange Membranes. *ACS Macro Lett.* **2022**, *11*, 1258–1264.

(33) Marioni, N.; Rajesh, A.; Zhang, Z.; Freeman, B. D.; Ganesan, V. What is the influ-

ence of ion aggregation and counterion condensation on salt transport in ion exchange membranes? *J. Membr. Sci.* **2024**, *701*, 122713.

(34) Lascaud, S.; Perrier, M.; Vallee, A.; Besner, S.; Prud'Homme, J.; Armand, M. Phase diagrams and conductivity behavior of poly (ethylene oxide)-molten salt rubbery electrolytes. *Macromolecules* **1994**, *27*, 7469–7477.

(35) Jorgensen, W. L.; Maxwell, D. S.; Tirado-Rives, J. Development and testing of the OPLS all-atom force field on conformational energetics and properties of organic liquids. *J. Am. Chem. Soc.* **1996**, *118*, 11225–11236.

(36) Jorgensen, W. L.; Tirado-Rives, J. Potential energy functions for atomic-level simulations of water and organic and biomolecular systems. *Proc. Natl. Acad. Sci. U.S.A.* **2005**, *102*, 6665–6670.

(37) Zeron, I.; Abascal, J.; Vega, C. A force field of Li^+, Na^+, K^+, Mg^{2+}, Ca^{2+}, Cl^-, and SO_4^{2-} in aqueous solution based on the TIP4P/2005 water model and scaled charges for the ions. *J. Chem. Phys.* **2019**, *151*, 134504.

(38) Sambasivarao, S. V.; Acevedo, O. Development of OPLS-AA force field parameters for 68 unique ionic liquids. *J. Chem. Theory Comput.* **2009**, *5*, 1038–1050.

(39) Doherty, B.; Zhong, X.; Gathiaka, S.; Li, B.; Acevedo, O. Revisiting OPLS force field parameters for ionic liquid simulations. *J. Chem. Theory Comput.* **2017**, *13*, 6131–6145.

(40) Abascal, J. L.; Vega, C. A general purpose model for the condensed phases of water: TIP4P/2005. *J. Chem. Phys.* **2005**, *123*, 234505.

(41) Lorenz, M.; Kilchert, F.; Nürnberg, P.; Schammer, M.; Latz, A.; Horstmann, B.; Schönhoff, M. Local volume conservation in concentrated electrolytes is governing charge transport in electric fields. *J. Phys. Chem. Lett.* **2022**, *13*, 8761–8767.

(42) Harris, K. R.; Kanakubo, M. Effect of Relative Mass on Ion Velocity Cross-Correlations in Ionic Liquids and Molten Salts: Different Perspectives in Different Reference Frames. *J Phys. Chem. B* **2024**, *128*, 4504–4512.

For Table of Contents Only

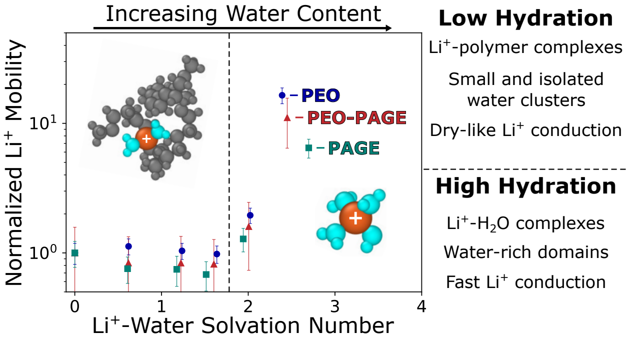

Supporting Information: What is the Role of Relative Humidity on Conductivity in Polymer Electrolytes?

Nico Marioni,[†] Akhila Rajesh,[†] Rahul Sujanani,[‡] Zidan Zhang,[†] Leo W. Gordon,[¶] Raphaële J. Clément,[¶] Rachel A. Segalman,[¶,‡] Benny D. Freeman,[†] and Venkat Ganesan[*,†]

†McKetta Department of Chemical Engineering, The University of Texas at Austin, Austin, Texas 78712, United States

‡Department of Chemical Engineering, University of California Santa Barbara, Santa Barbara, California 93106, United States

¶Materials Department and Materials Research Laboratory, University of California Santa Barbara, Santa Barbara, California 93106, United States

E-mail: venkat@che.utexas.edu

S1 Model and Methodology

Atomistic molecular dynamics (MD) simulations were performed on salt-doped polyethers under low hydration conditions using the GROMACS 2020.5 MD package.[S1,S2] The all-atom optimized potentials for liquid simulations (OPLS-AA),[S3,S4] Madrid,[S5] OPLS-2009IL,[S6,S7] and TIP4P-2005[S8] force field parameterizations were chosen to model the polymer, lithium (Li^+), bis(trifluoromethane)sulfonimide (TFSI^-), and water, respectively.

In the OPLS-AA parameterization, the net potential energy is expressed as the sum of bonded and non-bonded potentials.[S9] The bonded potential, U_b, is given by the following expression:

$$U_\mathrm{b} = \sum_b \frac{k_b}{2}(b-b_0)^2 + \sum_\theta \frac{k_\theta}{2}(\theta-\theta_0)^2 + \sum_\phi \sum_{n=0}^{5} (-1)^n C_n (\cos\phi)^n + \sum_\psi k_\psi (1+\cos(n\psi-\psi_0)), \tag{S1}$$

and includes contributions from the intermolecular bond, angle, dihedral, and improper dihedral interactions, where k_n are spring constants, C_n are Ryckaert-Bellemans potential constants, b are bond lengths, θ are bond angles, ϕ are dihedral angles, and ψ are improper dihedral angles. The equilibrium bond lengths, angles, and improper dihedral angles are given by b_0, θ_0, and ψ_0, respectively. The non-bonded potential, U_nb, is given by:

$$U_\mathrm{nb} = \sum_{i,j} f_{ij} \left\{ \frac{e^2 z_i z_j}{4\pi\epsilon_0 r_{ij}} + 4\epsilon_{ij} \left[\left(\frac{\sigma_{ij}}{r_{ij}}\right)^{12} - \left(\frac{\sigma_{ij}}{r_{ij}}\right)^{6} \right] \right\}, \tag{S2}$$

and is modeled as the sum of the electrostatic and Lennard-Jones (LJ) interactions scaled by f_{ij}, where f_{ij} is 0 for 1,2 and 1,3 interactions, 0.5 for 1,4 interactions, and 1 otherwise. LJ interaction parameters are determined using geometric mixing rules,[S9] $\sigma_{ij} = (\sigma_i\sigma_j)^{1/2}$ and $\epsilon_{ij} = (\epsilon_i\epsilon_j)^{1/2}$. $\mathrm{Li}^+ - \mathrm{Li}^+$, $\mathrm{Li}^+ - \mathrm{TFSI}^-$ and Li^+-water interaction parameters are determined using the Lorentz-Berthelot mixing rules,[S10] $\sigma_{ij} = (\sigma_i + \sigma_j)/2$ and $\epsilon_{ij} = (\epsilon_i\epsilon_j)^{1/2}$, as specified by Zeron et al.[S5]

Newton's equations of motion are integrated using the leap-frog Verlet integration scheme.[S11]

LJ and electrostatic interactions are computed in real space up to a 1.2 nm cutoff. Beyond 1.2 nm, long range electrostatic interactions are computed in reciprocal Fourier space with the fast smooth Particle-Mesh-Ewald (PME) algorithm[S12,S13] with a tolerance of 10^{-5}. All bonds that contain hydrogen atoms are constrained by the LINear Constraint Solver (LINCS) algorithm.[S14]

S1.1 Force Field Parameters

Figure S1 displays the atom naming scheme for (A) PEO, (B) PEO-PAGE, and (C) PAGE polymers. Li^+ ions, $TFSI^-$ atoms, water oxygen atoms, and water hydrogen atoms are represented by Li^+, TFSI-X, Ow, and Hw, respectively, where X is sulfur, nitrogen, oxygen, carbon, or fluorine (S, N, O, C, or F). Atom names are associated with their GROMACS atom type, LJ interaction parameters ($\sigma_{ii}, \epsilon_{ii}$), and atomic partial charges (q) in Table S1. To maintain electroneutrality with Li^+ ions from the Madrid model,[S5] $TFSI^-$ atomic partial charges are scaled by a factor of 0.85. GROMACS atom types are associated with their bond, angle, dihedral, and improper dihedral force field parameters in Tables S2-S5.

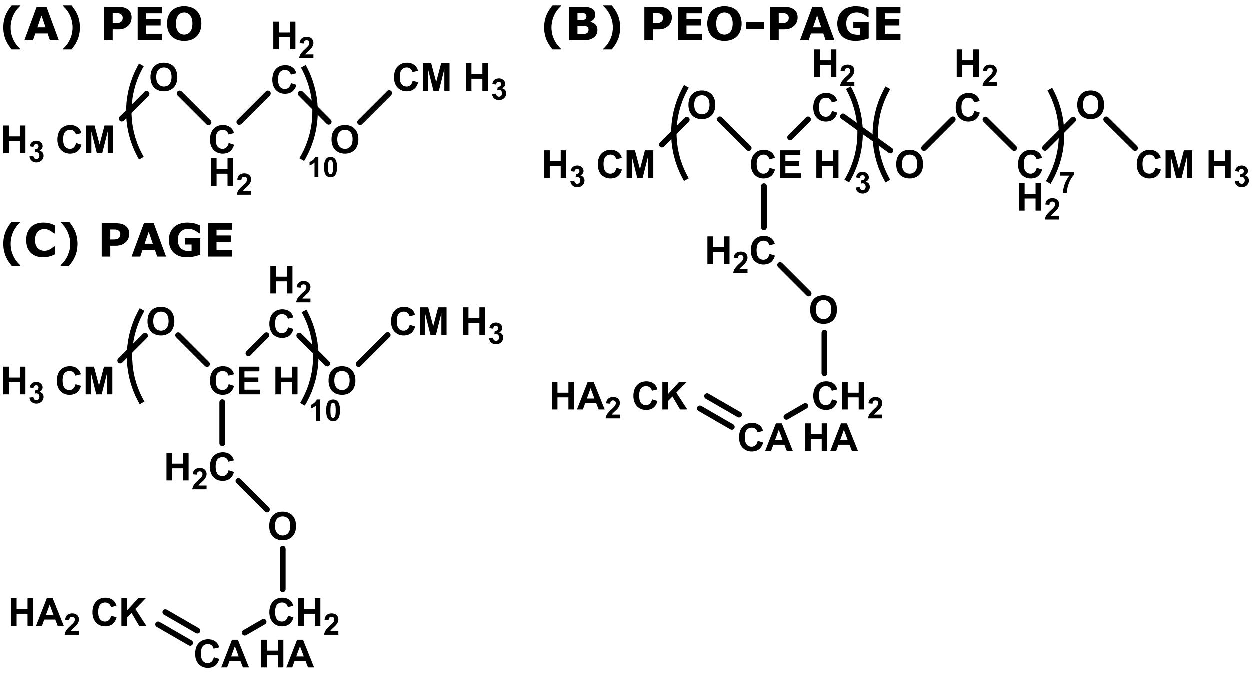

Figure S1: Atom naming scheme for (A) PEO, (B) PEO-PAGE, and (C) PAGE polymers.

Table S1: Atom type, Lennard-Jones parameters, and partial charges. The dashes indicate that the value from the previous line is repeated.

Atom Name	Atom Type	σ_{ii} (nm)	ϵ_{ii} (kJ/mol)	q
O	OT	0.290	0.58576	-0.400
C	CT	0.350	0.276144	0.140
CM	CT	-	-	0.110
CE	CT	-	-	0.170
CA	CM	0.355	0.317984	-0.115
CK	CM	-	-	-0.230
H	HT	0.250	0.12552	0.030
HA	HT	0.242	-	0.115
Li^+		0.14397	0.43508986	0.850
TFSI – F	TF	0.295	0.22175	-0.136
TFSI – C	TC	0.350	0.27614	0.2975
TFSI – S	TS	0.355	1.04600	0.867
TFSI – O	TO	0.296	0.87864	-0.4505
TFSI – N	TN	0.325	0.71128	-0.561
Ow[a]	OW	0.31589	0.77490765	-1.1128
Hw	HW	0.000	0.000	0.5564

[a] Charge is carried by a “dummy” atom in TIP4P-2005

Table S2: Equilibrium bond lengths and spring constants.

Atom Types	b_0 (nm)	k_b (kJ/mol/nm^2)
CT – OT	0.141	2.678e5
CT – CT	0.152	2.242e5
CT – HT	0.109	2.845e5
CM – CM	0.134	4.594e5
CM – CT	0.151	2.653e5
CM – HT	0.108	2.845e5
OW – HW	0.09572	5.024e5
TN – TS	0.1570	3.137e5
TS – TO	0.1437	5.331e5
TS – TC	0.1818	1.950e5
TC – TF	.1323	3.698e5

Table S3: Equilibrium bond angles and spring constants. The dashes indicate that the value from the previous line is repeated.

Atom Types	θ_0 (°)	k_θ (kJ/mol/rad^2)
CA – CT – CT	109.5	418.400
CT – OT – CT	-	502.080
HT – CT – OT	-	292.880
CT – CT – HT	110.7	313.800
HT – CT – HT	107.8	276.144
CM – CM – CT	124.0	585.760
CM – CT – OT	120.0	-
CM – CM – HT	-	292.880
CM – CT – HT	109.5	-
CT – CM – HT	117.0	-
HT – CM – HT	-	-
HW – OW – HW	104.52	628.020
TN – TS – TO	113.6	789.000
TN – TS – TC	103.5	764.000
TS – TC – TF	111.7	694.000
TS – TN – TS	125.6	671.000
TC – TS – TO	102.6	870.000
TO – TS – TO	118.5	969.000
TF – TC – TF	107.1	781.000

Table S4: Ryckaert-Bellemans dihedral potential constants. The dashes indicate that the value from the previous line is repeated.

Atom Types	(kJ/mol) C_0	(kJ/mol) C_1	(kJ/mol) C_2	(kJ/mol) C_3	(kJ/mol) C_4	(kJ/mol) C_5
CT – CT – CT – OT	2.874	0.582	2.092	-5.548	0.000	0.000
CT – CT – OT – CT	1.715	2.845	1.046	-5.607	-	-
CM – CT – OT – CT	-	-	-	-	-	-
CM – CM – CT – OT	1.046	-	-1.046	-	-	-
OT – CT – CT – OT	-1.151	1.151	0.000	0.000	-	-
CT – OT – CT – HT	1.590	4.770	-	-6.360	-	-
HT – CT – CT – OT	0.980	2.937	-	-3.916	-	-
CT – CT – CT – HT	0.627	1.882	-	-2.510	-	-
CM – CM – CT – HT	-0.778	-2.335	-	3.113	-	-
HT – CM – CT – HT	0.665	1.996	-	-2.661	-	-
HT – CM – CT – OT	0.979	2.937	-	-3.916	-	-
X – CM – CM – X[a]	58.576	0.000	-58.576	0.000	-	-
TN – TS – TC – TF	0.661	1.983	0.000	-2.644	-	-
TS – TN – TS – TO	-0.0075	-0.0225	-	0.030	-	-
TO – TS – TC – TF	0.7255	2.1765	-	-2.902	-	-
TS – TN – TS – TC	4.369	-21.179	10.420	6.390	-	-

[a] X represents any atom

Table S5: Improper dihedral constants.

Atom Types	ψ_0 (°)	k_ψ (kJ/mol/rad^2)	n
Z – CM – X – Y[a]	180.0	62.760	2

[a] X, Y, and Z represent any atom

S1.2 Systems

All systems are summarized in Table S6, where $r = N_{\mathrm{Salt}}/N_{\mathrm{Monomer}}$ is the salt loading, C_{Salt} is the average molar salt concentration relative to the system volume, w_u is the water uptake in g water/g salt-doped polymer, and N_{Polymer}, N_{Salt}, and $N_{\mathrm{H_2O}}$ are the number of polymer chains (10 monomers per chain), salt pairs, and water molecules, respectively. N_{Monomer} is the number of monomer units in the system, equivalenty $10N_{\mathrm{Polymer}}$ for 10-mer polymers. Five independent simulations are performed at each specification.

Table S6: Simulation setups. The dashes indicate that the value from the previous line is repeated.

Polymer	r	C_{Salt} (M)	w_u	$N_{\text{H}_2\text{O}}/N_{\text{Li+}}$	N_{Polymer}	N_{Salt}	$N_{\text{H}_2\text{O}}$
PEO	0.045	0.82	0.000	0.000	580	261	0
-	-	0.80	0.018	1.39	560	252	350
-	-	0.78	0.037	2.78	540	243	675
-	-	0.77	0.049	3.71	-	-	902
-	-	0.75	0.073	5.56	520	234	1300
PEO	0.10	1.60	0.000	0.000	520	520	0
-	-	1.57	0.015	0.625	-	-	325
-	-	1.54	0.029	1.25	509	509	637
-	-	1.52	0.039	1.67	503	503	841
-	-	1.48	0.058	2.50	490	490	1225
-	-	1.35	0.116	5.00	455	455	2275
PEO-PAGE	0.045	0.58	0.000	0.000	402	181	0
-	-	0.58	0.014	1.39	396	179	248
-	-	0.57	0.027	2.78	390	176	488
-	-	0.56	0.037	3.71	386	174	644
-	-	0.55	0.055	5.56	378	171	945
PEO-PAGE	0.10	1.19	0.000	0.000	362	362	0
-	-	1.17	0.011	0.625	-	-	227
-	-	1.15	0.023	1.25	357	357	447
-	-	1.14	0.031	1.67	353	353	590
-	-	1.12	0.046	2.50	347	347	868
-	-	1.06	0.092	5.00	329	329	1645
PAGE	0.045	0.35	0.000	0.000	240	108	0
-	-	0.35	0.008	1.39	-	-	149
-	-	0.35	0.017	2.78	236	107	295
-	-	0.34	0.023	3.71	235	106	392
-	-	0.34	0.034	5.56	232	105	580
PAGE	0.10	0.74	0.000	0.000	226	226	0
-	-	0.73	0.008	0.625	-	-	142
-	-	0.73	0.015	1.25	224	224	280
-	-	0.72	0.020	1.67	223	223	373
-	-	0.71	0.031	2.50	220	220	550
-	-	0.69	0.061	5.00	213	213	1065

The polymer chains, salt pairs, and water molecules are randomly packed into the initial simulation box in the gas phase. A multi-step equilibration procedure, based on work by Abbot et al.,[S15] is used to obtain an equilibrated state before the production run (Table S7). The compression and pre-equilibration are performed with a 1 fs timestep, and the temperature and pressure are coupled by a Berendsen thermostat and barostat[S16] with 0.5 ps coupling constants. The compression scheme (step 2) is repeated until the density reaches 0.95 g/cm^3 (chosen to be below the equilibrium density), followed by an NVT simulation (step 3) at this low density to allow for more conformations to be sampled. Steps 4-6 are repeated eight times at each pressure indicated to converge the system density. The equilibration and production simulations are performed with a 1 fs and 2 fs timestep, respectively, and the temperature and pressure are coupled by a velocity-rescale thermostat[S17] and Parrinello-Rahman barostat[S18,S19] with 1 ps coupling constants. All systems have a final simulation box size of $L \sim 8$ nm, where L is the length of the cubic simulation box.

Table S7: Simulation procedure.

Step	Simulation Conditions	Simulation Time
1	Energy minimization	Steepest Descent
2^a	NPT 400 K, 500 bar	5 ps
3^b	NVT 1000 K	600 ps
4^b	NVT 1000 K	250 ps
5^b	NVT 400 K	500 ps
6^b	NPT 400 K, [1000, 10000, 5000, 1000, 500, 100, 10 1*] bar	250 ps, 2 ns*
7^c	NPT 400 K, 1 bar	15 ns
8^d	NVT 400 K	200 ns
9^e	NVT 400 K, $E = [0.02, 0.04, 0.06, 0.08, 0.10]$ V/nm	50 ns

[a] Compression: repeat until system reaches a density of 0.95 g/cm^3

[b] Pre-equilibration: repeat steps 4-6 for each pressure specified; * denotes longer simulations

[c] Equilibration; [d] Production

[e] Non-equilibrium production: perform simulation under each electric potential specified

To probe ion conduction,[S20,S21] each system is simulated under the influence of an electric field. Following the production simulation (step 8), each system is simulated under non-equilibrium conditions with an electric potential, E, applied simultaneously in the x, y, and z directions (See Section S2.1 for more details). The non-equilibrium productions (step 9) are performed with a 2 fs timestep, and the temperature is coupled by a velocity-rescale thermostat with 1 ps coupling constant. Each electric potential is probed using five independent simulations at each condition recorded in Table S6.

S2 Methods of analysis

S2.1 Ionic mobilities and conductivity

Ionic mobilities and conductivities were computed from non-equilibrium MD simulations under the influence of an electric field. At long time, ions reach a steady state drift velocity in the direction of an applied electric potential. The drift velocities were computed as:

$$v_i^x = \lim_{t\to\infty} \frac{d}{dt} \langle x_i^\alpha(t+t_0) - x_i^\alpha(t_0)\rangle_E, \tag{S3}$$

where v_i^x is the steady state drift velocity of species i in the x direction, $x_i^\alpha(t)$ is the x position of atom α of species i at time t, and $\langle\rangle_E$ denotes the ensemble average over all atoms and time t_0 under the influence of an electric potential E. As mentioned in Section S1.2, the electric potential is applied in the x, y, and z directions simultaneously, where each axis may be analyzed independently (assuming a homogeneous, bulk system) for one-directional transport due to the presence of an electric field.[S22] Therefore, we measure $\langle v_i\rangle_E$, which represents the ensemble average drift velocity over all coordinate axes, v_i^x, v_i^y, and v_i^z, under the influence of E, greatly improving statics compared to single field simulations. $\langle v_i\rangle_E$ were calculated from linear fits over $t = 10 - 40$ ns described by a log-log slope of $m = 1 \pm 0.01$ and coefficient of determination $R^2 \geq 0.999$.

The ionic mobility is defined as:[S20,S21]

$$\mu_i = \frac{\langle v_i\rangle_E}{q_s E}, \tag{S4}$$

where μ_i is the average ionic mobility of species i and q_s is the charge scale factor. As discussed in Section S1.1, the ionic charge of Li^+ and $TFSI^-$ are scaled by a factor of

$q_s = 0.85$. Therefore, the electric potential must be scaled by the same factor to account for the artificially lower electrical force felt by the ions. Ionic mobilities are measured relative to the polymer-fixed reference frame. See Section S3 for more information on other reference frame analyses.

To obtain values analogous to experimentally measured conductivities, we must calculate μ_i within the linear response regime, where the electric potential does not significantly disturb the system from its equilibrium behavior. Therefore, we measured $\langle v_i \rangle_E$ across five electric potentials, $E = 0.02, 0.04, 0.06, 0.08, 0.10$ V/nm, where $\langle v_i \rangle_E$ must vary linearly as a function of E within the linear response regime. We observe good linearity for $E = 0.02 - 0.06$ V/nm for all systems, so all linear fits for μ_i are limited to this range of field strengths. Figure S2 displays the Li^+ and TFSI^- drift velocities as a function of E for (A,B) PEO, (C,D) PEO-PAGE, and (E,F) PAGE systems at $r =$ (A,C,E) 0.045 and (B,D,F) 0.10 Li^+ ions per monomer. The dashed and dash-dotted lines represent the linear regression fit over $E = 0.02 - 0.06$ V/nm for Li^+ and TFSI^- ions, respectively, where the slope is the ionic mobility. We note that the data points for $E = 0.10$ V/nm generally do not lie within the linear response regime, while the values for $E = 0.08$ V/nm do for some systems and don't for others, rationalizing our decision to restrict data fitting to $E = 0.02 - 0.06$ V/nm.

From Equation 1 in the main paper, the molar conductivity, Λ_m, can be calculated from the sum of the individual ionic mobilities scaled by their ionic charge. We note that the ionic charge, z_i, is not scaled by q_s when calculating Λ_m, i.e., $z_{\text{Li}^+} = 1$ and $z_{\text{TFSI}^-} = -1$. While the ionic charges are scaled in simulations to mimic polarizability,[S5,S23] the transport of ions under an electric field represents the motion of fully charged ions. For completeness, Figure S3 displays the (A) molar conductivity, (B) TFSI^- mobility, and (C) Li^+ mobility as a function of $N_{\text{H}_2\text{O}}/N_{\text{Li}^+}$.

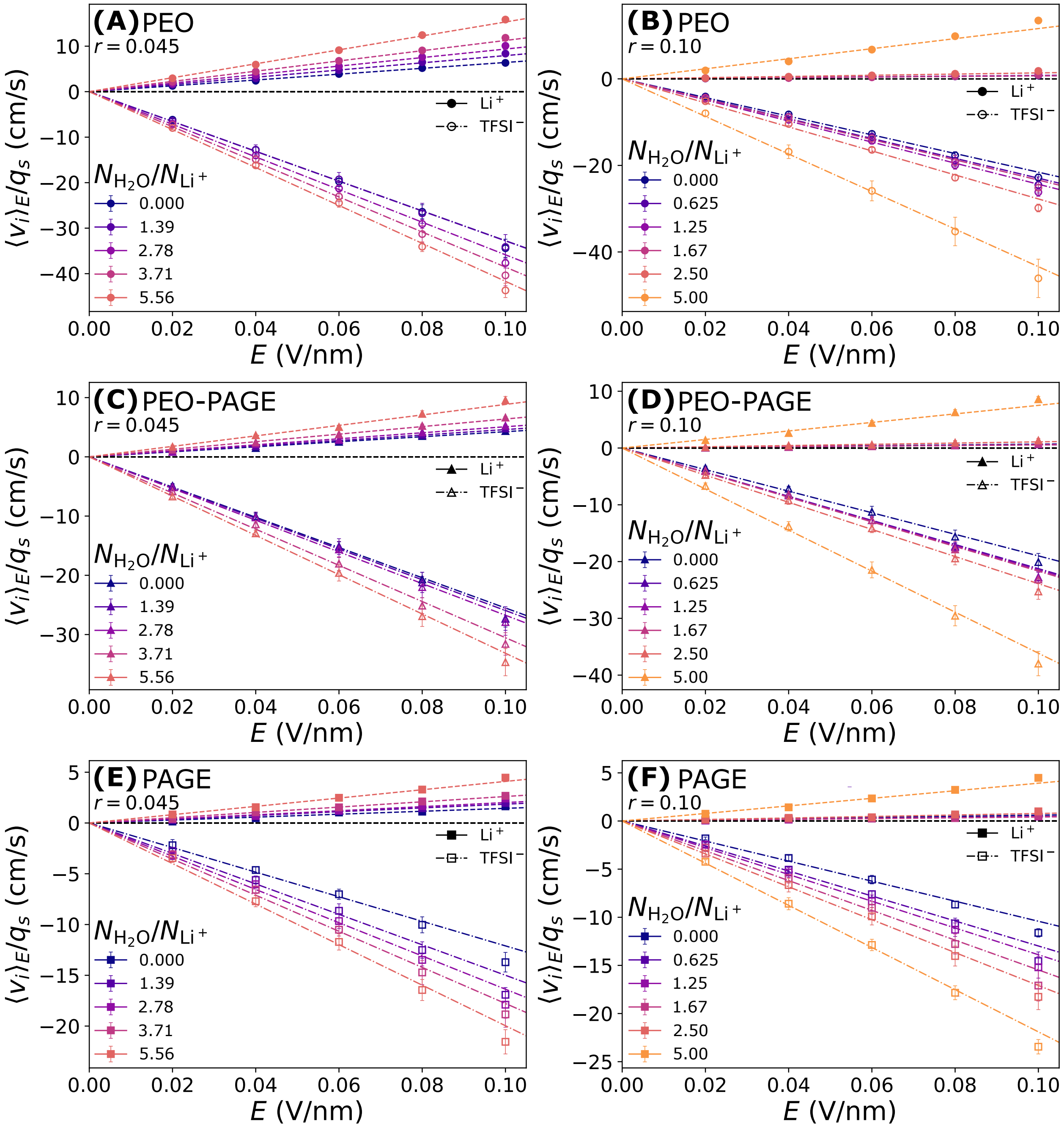

Figure S2: Li^+ and $TFSI^-$ drift velocities as a function of electric potential for (A,B) PEO, (C,D) PEO-PAGE, and (E,F) PAGE systems at $r =$ (A,C,E) 0.045 and (B,D,F) 0.10 Li^+ ions per monomer. The dashed and dash-dotted lines represent the linear regression fit over $E = 0.02 - 0.06$ V/nm for Li^+ and $TFSI^-$ ions, respectively.

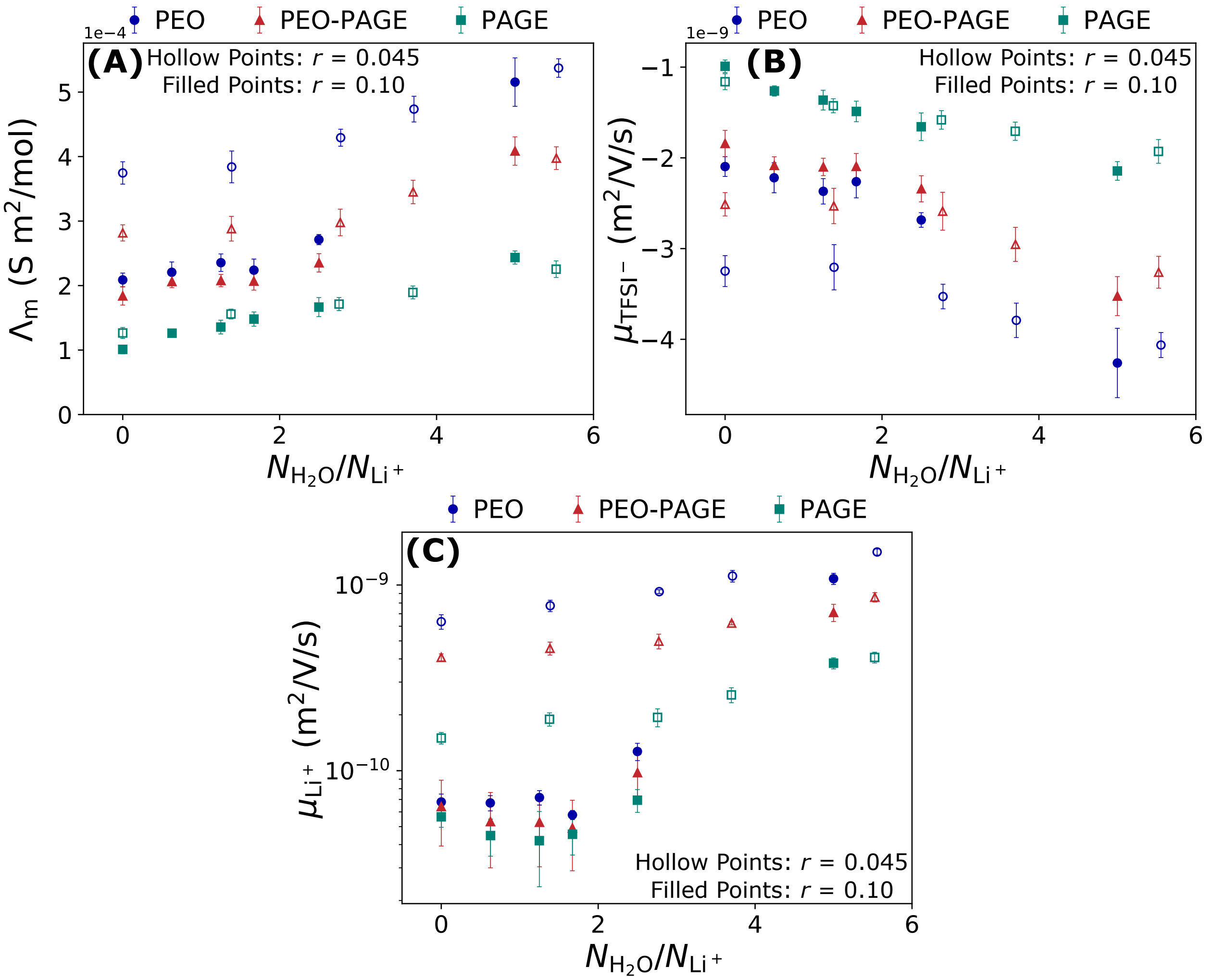

Figure S3: (A) Molar conductivity, (B) TFSI$^-$ mobility, and (C) Li$^+$ mobility as a function of the number of water molecules per Li$^+$ ion. Hollow and filled points represent systems at lower ($r = 0.045$) and higher ($r = 0.10$) salt loadings, respectively.

S2.1.1 Comparison to Experiments

Figure S4 compares the experimental (adapted with permission from Sujanani et al.[S24]) and simulated molar conductivities normalized to their respective values under dry conditions as a function of N_{H_2O}/N_{Li^+} for (A,B) PAGE and (C) PEO-PAGE systems at r = (A,C) 0.045 and (B) 0.10 Li$^+$ ions per monomer. Experimental systems are studied at room temperature with approximately 90- and 160-mer polymer chains for PAGE and PEO-PAGE, respectively (approximately 10,000 g/mol molecular weight). By contrast, simulated systems are studied at 400 K with 10-mer polymer chains (approximately 1,140 and 650 g/mol molecular weight for PAGE and PEO-PAGE, respectively). Despite these differences, we observe qualitative agreement between experiments and simulations. Specifically, we observe a relatively linear increase in the molar conductivity as a function of $N_{\mathrm{H_2O}}/N_{\mathrm{Li^+}}$ for PAGE systems at both salt loadings, and a non-linear increase in conductivity as a function of water content for PEO-PAGE systems at $r = 0.045$. Comparing PAGE systems at low and high salt loading, we observe a more significant increase in conductivity relative to dry conditions at $r = 0.10$ compared to systems at $r = 0.045$. We note that experimental conductivities, especially for the PEO-PAGE chemistry, increase more as a function of water content than simulations. We expect this may arise due to limitations of the computational model, or the difference in temperature and polymer molecular weight between experiments and simulations (see below for more discussion of the latter). However, the qualitative trend is maintained, so the underlying physics is consistent between experiments and simulations.

Next, we examine to the impact of polymer molecular weight. Experimental studies on ionic conductivity with varying polymer molecular weight in LiTFSI-doped PEO have shown a decrease in conductivity with increasing molecular weight within the range of 190-10,000 g/mol (4-230 repeat units), with minimal impact at higher molecular weights (we note that this dependence does not change significantly as a function of temperature, supporting the assumption that the difference in temperature between simulations and experiments does not significantly impact the underlying physics).[S25] These two regimes are generally understood to arise due to two distinct mechanisms for ion transport: polymer segmental dynamics and ion-polymer vehicular transport, where the former is independent of the molecular weight and the latter is only present in low molecular weight polymer systems and serves to increase conductivity relative to high molecular weight systems. For the purpose of this study, we expect that vehicular transport does play a role in ion conduction within simulations, while such a mechanism will be relatively minimal in the experiments conducted by Sujanani et al.[S24]

However, of interest to this work is whether the dependence of ion conduction on hydra-

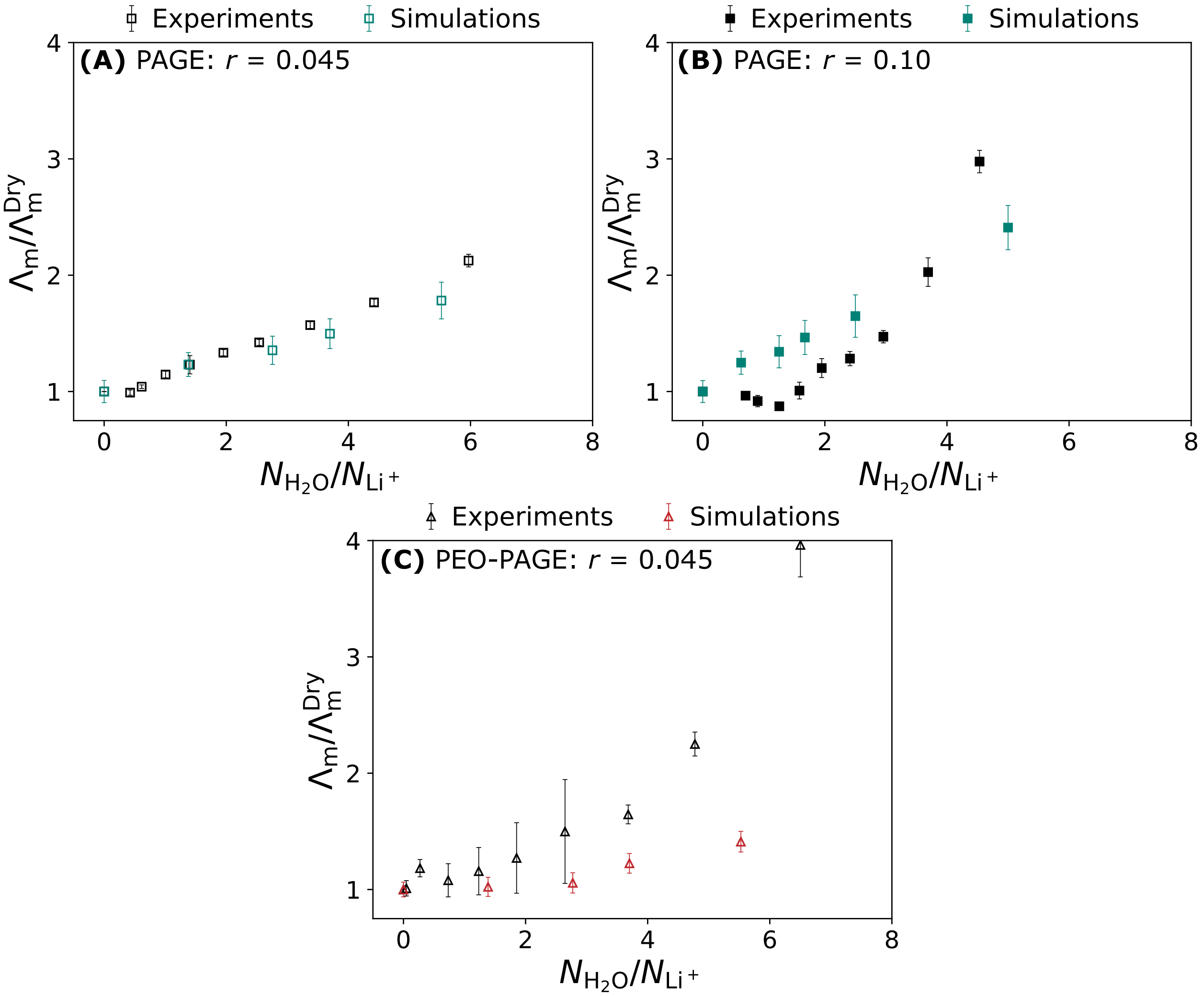

Figure S4: Comparison of the experimental and simulated molar conductivities normalized to their respective values under dry conditions as a function of the number of water molecules per Li^+ ion for (A,B) PAGE and (C) PEO-PAGE systems at r = (A,C) 0.045 and (B) 0.10 Li^+ ions per monomer. Experimental data adapted with permission from Sujanani et al.[S24] tion within the non-percolated regime significantly changes with polymer molecular weight. As discussed above, from Figure S4, we generally observe a stronger increase in the conductivity relative to the dry condition at high water contents in experiments compared to simulations. This may be rationalized by the lack of vehicular transport in experimental systems. As water content increases, Li^+ ions are increasingly solvated by water molecules and disassociate from the polymer chains. Therefore, we expect that the speedup of Li^+ transport relative to the dry case is stronger for systems with relatively immobile polymer chains (high molecular weight) compared to systems with diffusive polymer chains (low molecular weight). However, while we observe quantitative differences, the overall trends are in agreement with experiments and are not expected to significantly impact the mechanistic description of ion conduction in this study. Furthermore, we note that the discussion in the main paper focuses on the polymer-fixed reference frame for ionic mobilities. Under this reference frame, the polymer center-of-mass is assumed to be immobile. We expect that such an analysis more closely represents the experimental system with long, relatively immobile polymer chains.

S2.2 Ion solvation analysis

As described in our previous study,[S26] radial distribution functions (RDFs), $g_{i-j}(r)$, were computed to describe the static ion association between species i and j. The RDF is defined as the ratio of the local density of species j around species i relative to the bulk density of species j,[S27]

$$g_{i-j}(r) = \frac{V}{4\pi r^2 N_i N_j} \sum_i \sum_j \langle \delta(r - r_{i-j}) \rangle, \tag{S5}$$

where N_k is the number of molecules of species k, and δ is the Dirac delta function. From the RDF, the association distance, r^*_{i-j}, is obtained as the first minima of $g_{i-j}(r)$. This cutoff, or solvation shell, is used to delineate whether two specific ions/atoms of species i and j are associated ($r_{i-j} < r^*_{i-j}$) at a given time and permits us to characterize ion pairing/solvation.

To maintain a consistent definition of the Li^+ solvation shell with polymer, water, and $TFSI^-$, the Li^+ association distance is measured from the RDF between Li^+ and polymer, water, and $TFSI^-$ oxygen atoms, $g_{\mathrm{Li^+-O}}(r)$, where O represents all polymer O, water O, and $TFSI^-$ O atoms. As in previous work,[S26] $TFSI^-$ – water association is measured from the $TFSI^-$ sulfur – water oxygen RDF, $g_{\mathrm{TFSI^-\ S-H_2O\ O}}(r)$. Figures S5 and S6 present the Li^+ – oxygen and $TFSI^-$ sulfur – water oxygen RDFs, respectively, for (A,B) PEO, (C,D) PEO-PAGE, and (E,F) PAGE systems at $r =$ (A,C,E) 0.045 and (B,D,F) 0.10 Li^+ ions per monomer, where the first minima are used to delineate ion solvation.

Figure S7 displays a comparison of the (A) Li^+ – polymer oxygen, (B) Li^+ – water oxygen, and (C) Li^+ – $TFSI^-$ oxygen radial distribution function first peaks for PEO, PEO-PAGE, and PAGE at $r = 0.045$ (dashed lines) and 0.10 (solid lines) Li^+ ions per monomer as a function of $N_{\mathrm{H_2O}}/N_{\mathrm{Li^+}}$. We note that the Li^+ – $TFSI^-$ solvation peaks are significantly smaller compared to Li^+ – EO and Li^+ – H_2O (c.f. Figures S7C and S7A,B). Therefore, Li^+ – $TFSI^-$ ion pairing is relatively negligible (less than 10% of ions) and does not have a significant impact on ion conduction.

Figures S8 and S9 display the Li^+ – EO and Li^+ – H_2O solvation distributions for (A,B) PEO, (C,D) PEO-PAGE, and (E,F) PAGE systems at $r =$ (A,C,E) 0.045 and (B,D,F) 0.10 Li^+ ions per monomer, where EO represents polymer ether oxygen atoms. From Figure S8, Li^+ is solvated by 5-6 EO atoms under dry conditions for all systems. As water content increases, Li^+ – EO solvation shifts toward the left, with a favorable peak forming at two EO atoms. At higher water content, we observe a growing fraction of “free” Li^+ ions completely disassociated from the polymer chain ($n = 0$), where polymers with higher EO content (PEO > PEO-PAGE > PAGE) exhibit a smaller fraction of “free” Li^+ ions. This trend corresponds to increasing Li^+ – H_2O solvation, where we observe a favorable peak at two water molecules, and, at higher water contents, a growing peak of four solvating water molecules.

The shift from EO to water solvation of Li^+ ions may be understood by the significantly larger Li^+ – H_2O solvation (RDF) peak compared to Li^+ – EO (Figures S7A and B), where

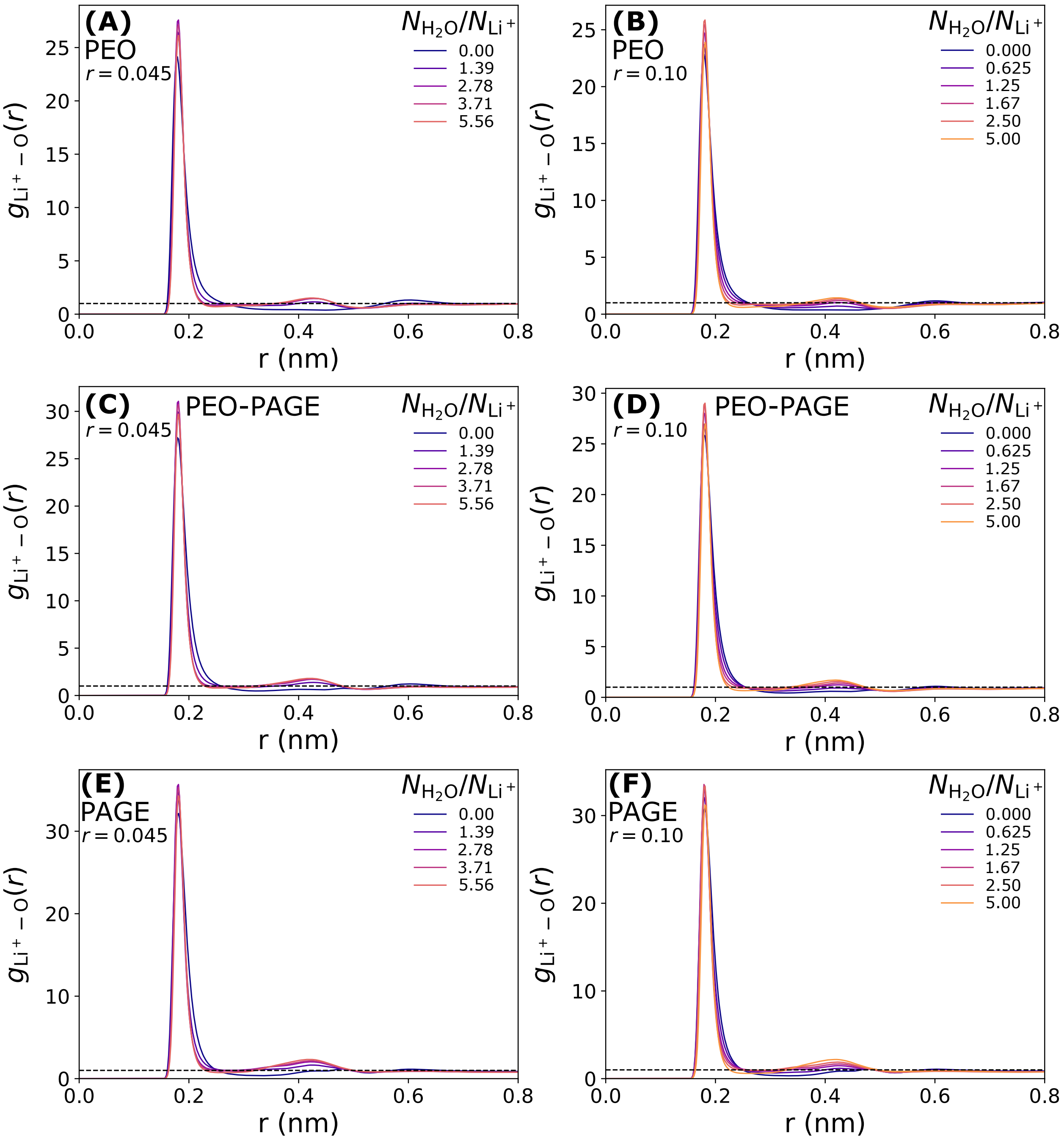

Figure S5: Li^+ − oxygen radial distribution functions for (A,B) PEO, (C,D) PEO-PAGE, and (E,F) PAGE systems at $r =$ (A,C,E) 0.045 and (B,D,F) 0.10 Li^+ ions per monomer. O represents polymer, water, and $TFSI^-$ oxygen atoms.

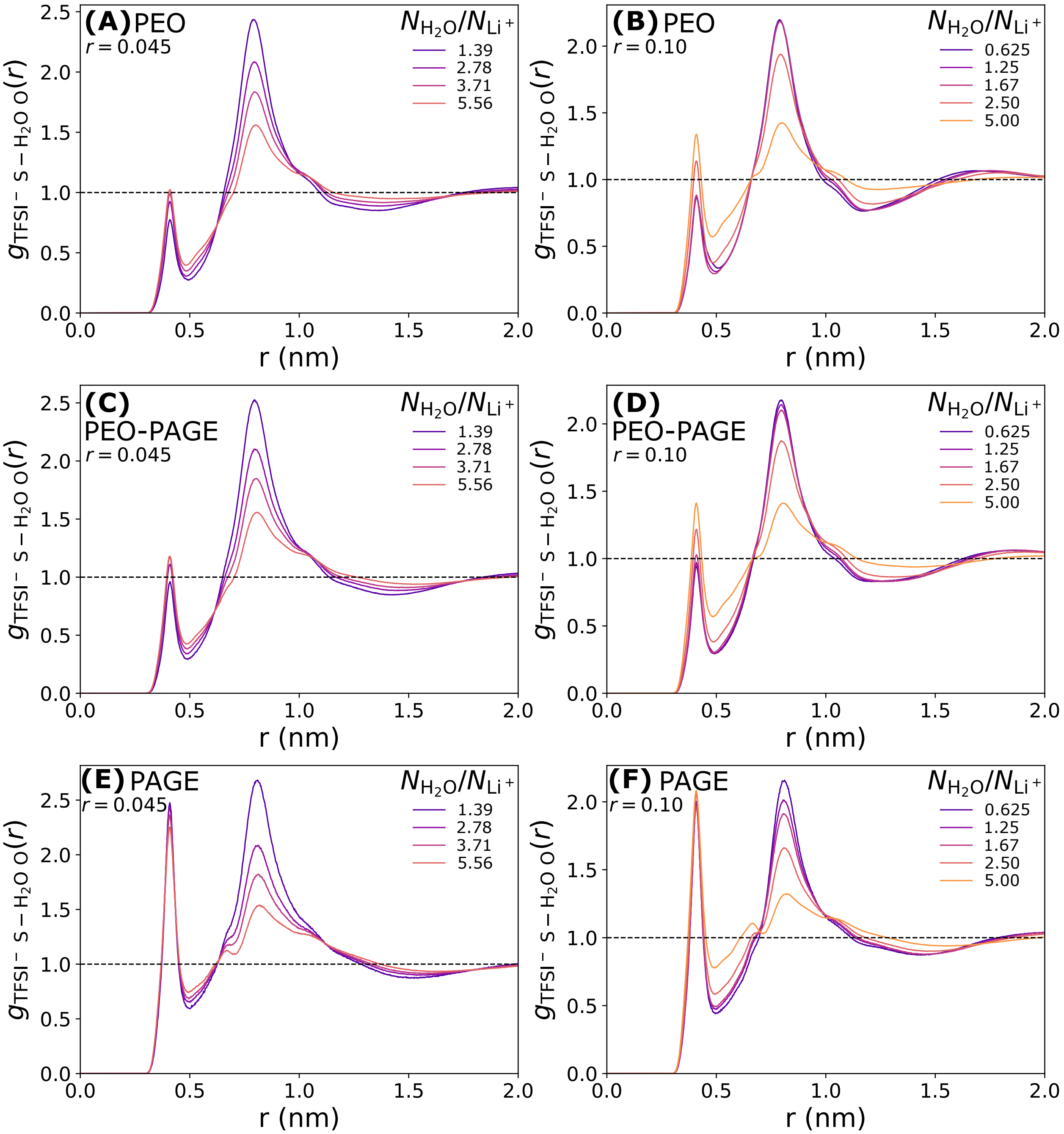

Figure S6: TFSI$^-$ sulfur – water oxygen radial distribution functions for (A,B) PEO, (C,D) PEO-PAGE, and (E,F) PAGE systems at r = (A,C,E) 0.045 and (B,D,F) 0.10 Li$^+$ ions per monomer. TFSI$^-$ S and H_2O O represent TFSI$^-$ sulfur and water oxygen atoms, respectively.

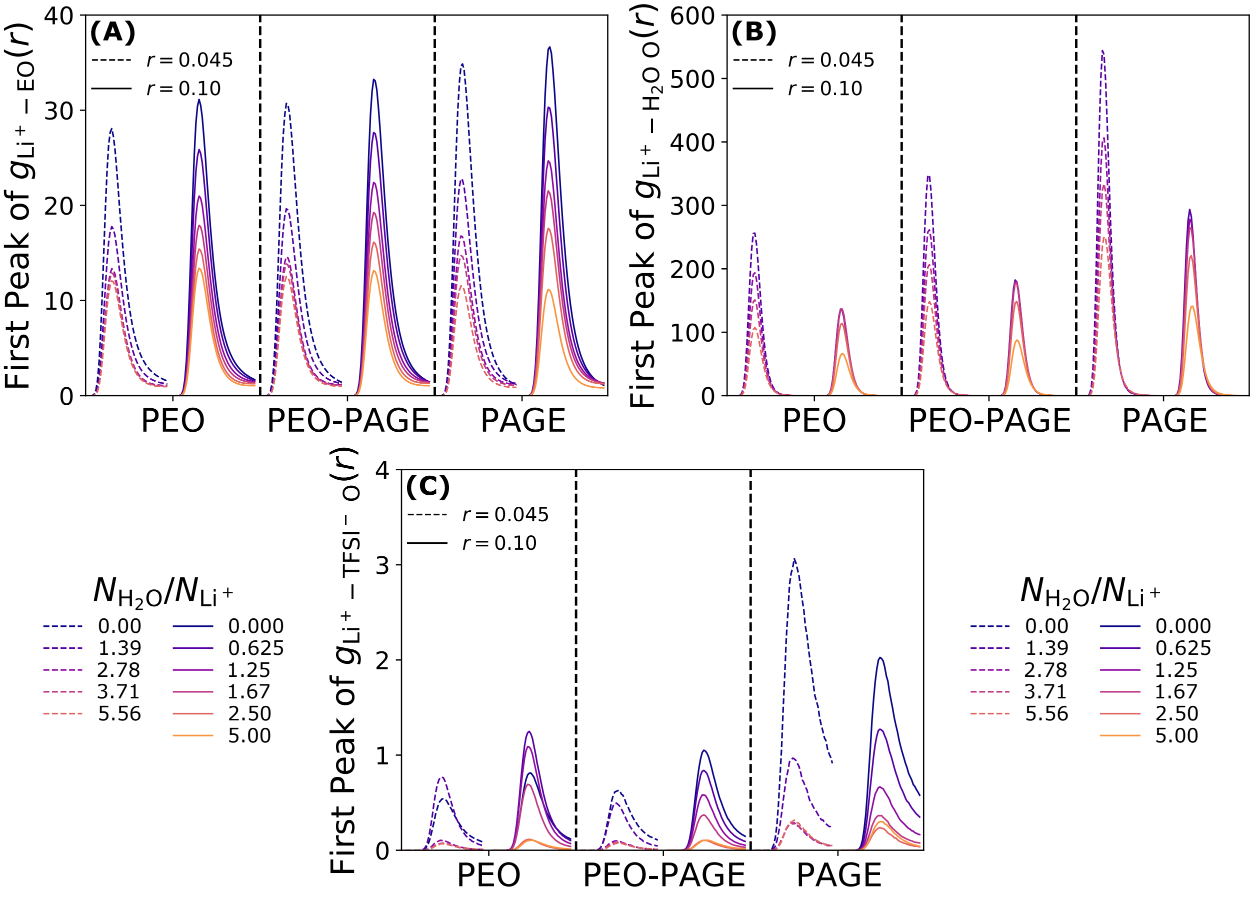

Figure S7: Comparison of the (A) $\mathrm{Li}^+ -$ polymer oxygen, (B) $\mathrm{Li}^+ -$ water oxygen, and (C) $\mathrm{Li}^+ - \mathrm{TFSI}^-$ oxygen radial distribution function first peaks for PEO, PEO-PAGE, and PAGE at $r = 0.045$ (dashed lines) and 0.10 (solid lines) Li^+ ions per monomer as a function of the number of water molecules per Li^+ ion.

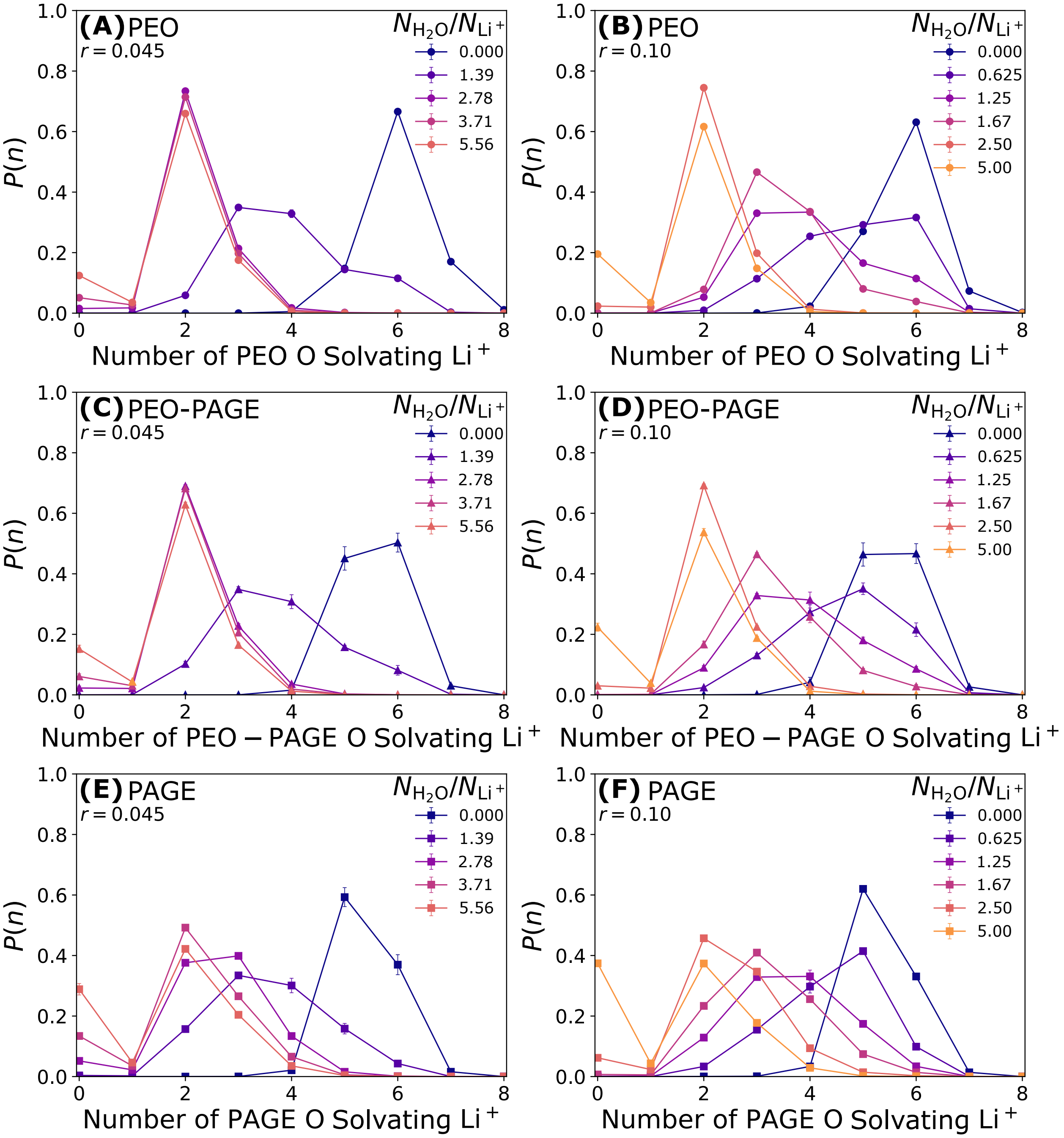

Figure S8: Li^+ − polymer oxygen solvation distributions for (A,B) PEO, (C,D) PEO-PAGE, and (E,F) PAGE systems at r = (A,C,E) 0.045 and (B,D,F) 0.10 Li^+ ions per monomer.

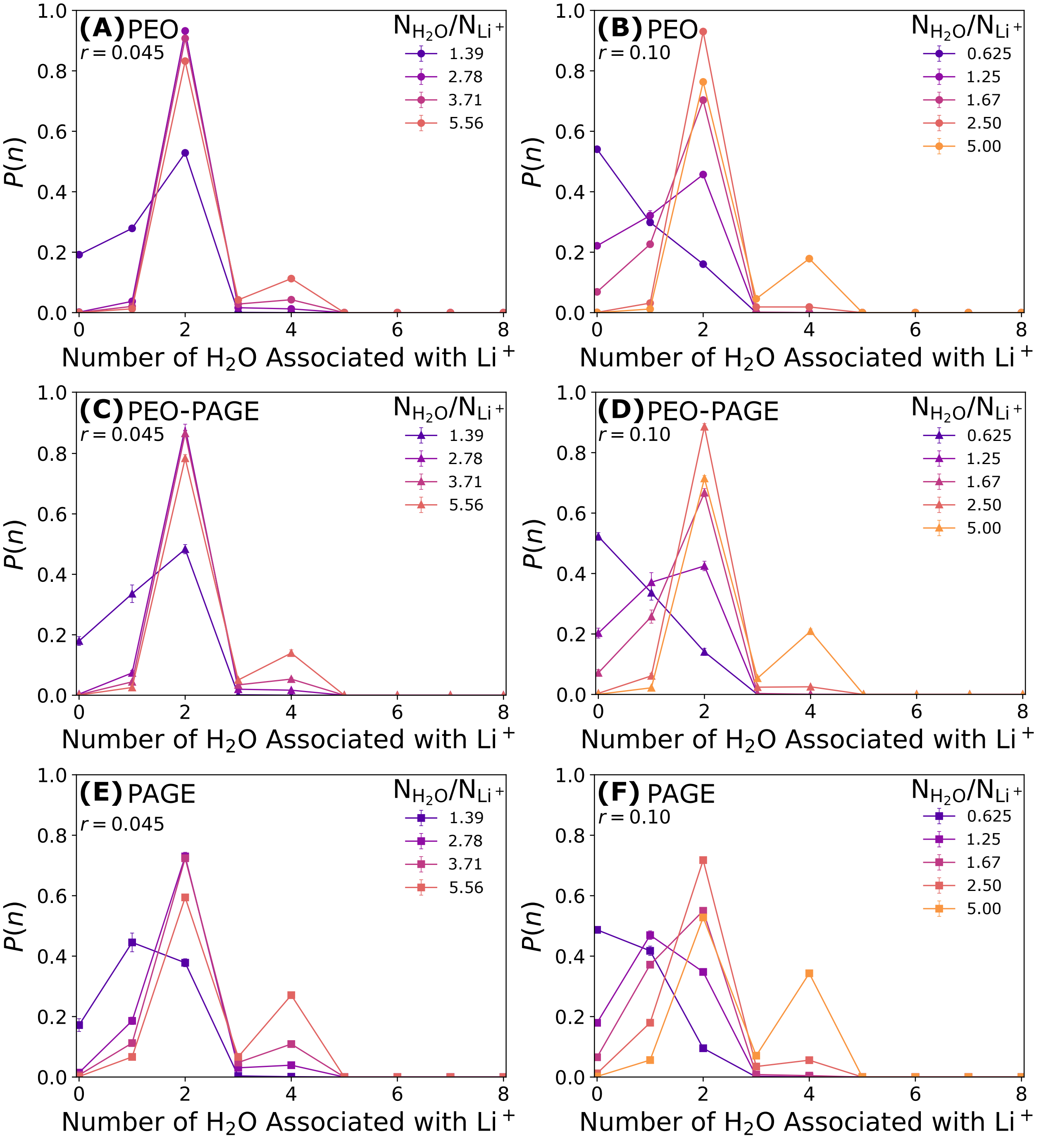

Figure S9: Li^+ − water oxygen solvation distributions for (A,B) PEO, (C,D) PEO-PAGE, and (E,F) PAGE systems at r = (A,C,E) 0.045 and (B,D,F) 0.10 Li^+ ions per monomer.

a higher peak value (at around the same solvation distance) indicates a stronger free energy of solvation. Furthermore, we attribute the increase in the fraction of "free" Li^+ ions at high water content with increasing AGE content to the relative ratios of these solvation peaks. Specifically, we observe much stronger $Li^+ - H_2O$ solvation peaks in PAGE systems compared to PEO at the same salt loading. In contrast, $Li^+ - EO$ solvation peaks are relatively similar. Therefore, Li^+ ions exhibit more favorable solvation with water compared to AGE EO atoms, leading to a higher fraction of "free" ions completely dissassociated from the polymer.

For completeness, Figure S10 displays the (A) $TFSI^-$ and (B) Li^+ hydration numbers as a function of N_{H_2O}/N_{Li^+}, where n_{i-H_2O} is the average number of water molecules solvating ions of species i.

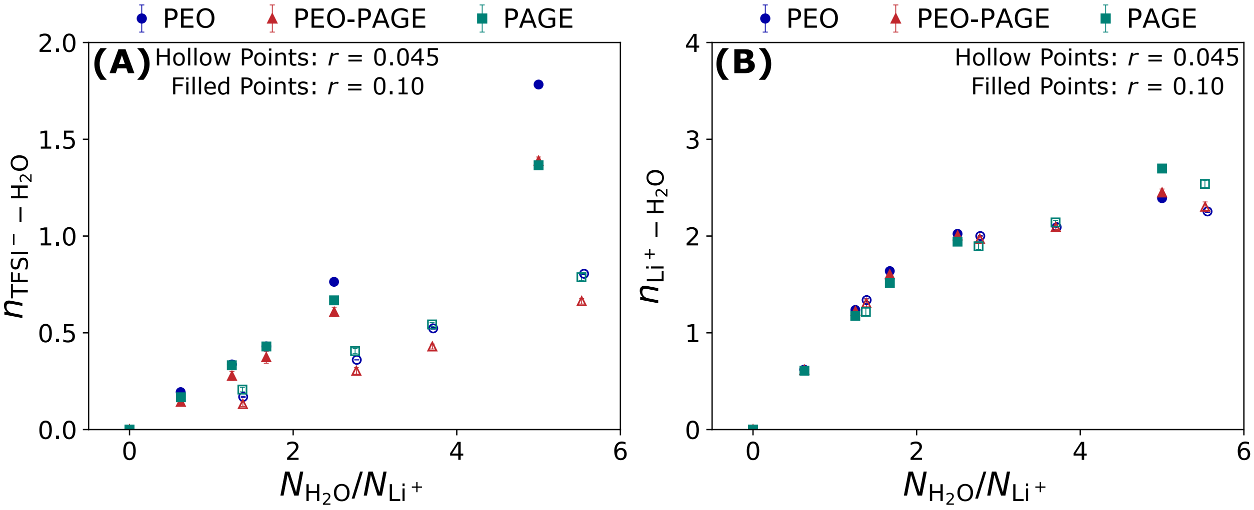

Figure S10: (A) $TFSI^-$ and (B) Li^+ hydration numbers as a function of the number of water molecules per Li^+ ion, where n_{i-H_2O} is the average number of water molecules solvating ions of species i. Hollow and filled points represent systems at lower ($r = 0.045$) and higher ($r = 0.10$) salt loadings, respectively.

S2.3 Water cluster analysis

As described in our previous study,[S26] water clusters are defined as groups of water molecules with overlapping water-water coordination shells ($r_{H_2O\ O-H_2O\ O} < r^*_{H_2O\ O-H_2O\ O}$) at a given timestep. For example, if the coordination shell of a water molecule α contains two water molecules β and γ (unassociated with each other), then β and γ are indirectly associated by their common association (overlapping coordination shell) with α. Furthermore, α is also indirectly associated with all other water molecules contained in the coordination shells of β and γ, etc. All water molecules directly associated via coordination shells and indirectly associated by overlapping coordination shells are defined as a water cluster. Figure S11 displays the probability, $P(n)$, that a water molecule is associated with a water cluster of size n for (A,B) PEO, (C,D) PEO-PAGE, and (E,F) PAGE systems at $r =$ (A,C,E) 0.045 and (B,D,F) 0.10 Li^+ ions per monomer. The water-water association distance $r^*_{\mathrm{H_2O\ O-H_2O\ O}} =$ 0.4 nm, where $\mathrm{H_2O}$ O represents water oxygen atoms.

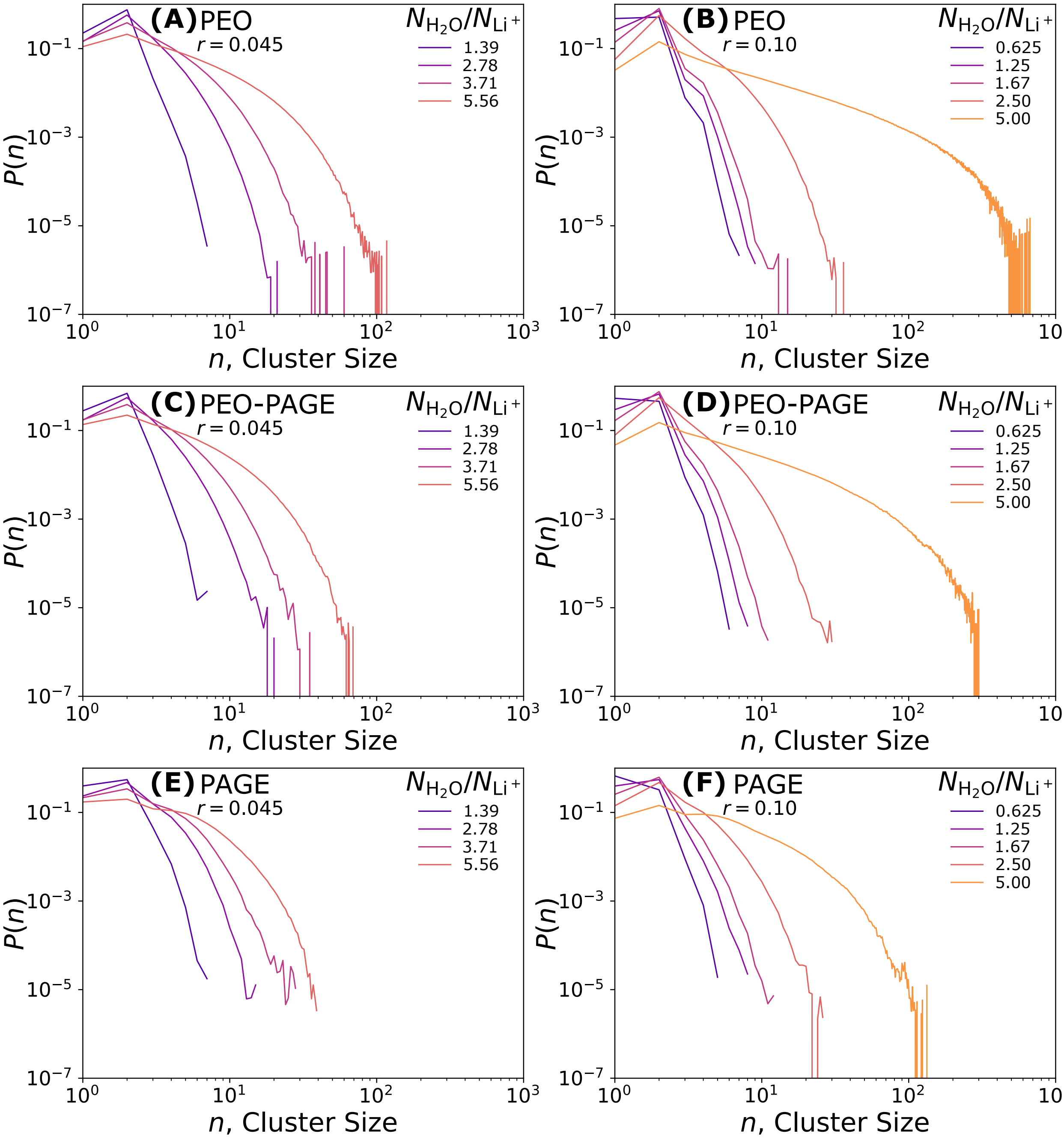

Figure S11: Probability that a water molecule is associated with a water cluster of size n for (A,B) PEO, (C,D) PEO-PAGE, and (E,F) PAGE systems at $r =$ (A,C,E) 0.045 and (B,D,F) 0.10 Li^+ ions per monomer.

S3 Reference Frame Analysis

As mentioned in the main paper and Section S2.1, ionic mobilities are measured relative to the polymer-fixed, i.e., polymer center of mass (P-CoM), reference frame, chosen to analyze the ionic mobilities under the assumption of approximately immobile (high molecular weight) polymer chains (See Section S2.1.1). However, there is some debate on the appropriate reference frame to apply when analyzing transport processes.[S28,S29] In Sections S3.1 and S3.2, we present results pertaining to the system center of mass (CoM) and system center of volume (CoV) reference frames, respectively, where the former is commonly applied in computational studies and the latter is argued to be equivalent to the experimental laboratory frame of reference.[S28] We note that ionic conductivity is reference frame independent. Therefore, the following analysis will focus on ionic mobilities.

S3.1 Center of Mass Reference Frame

Figure S12 presents the normalized (A,C) TFSI^- and (B,D,E) Li^+ mobilities measured relative to the system CoM reference frame analogously to the P-CoM reference frame data in Figures 1B,C, 2A,B, and 3D (corresponding to Figures S12A-E, respectively). For ease of comparison, all data is plotted using the same scale as in the main paper. In general, we observe consistent trends to those discussed in the main paper. Specifically, TFSI^- mobilities increase approximately linearly as a function of $N_{\mathrm{H_2O}}/N_{\mathrm{Li^+}}$ (cf. Figures S12A and 1B), and they exhibit a near-universal correlation to $n_{\mathrm{TFSI^-{-}H_2O}}$ (cf. Figures S12C and 2A). However, TFSI^- mobilities increase marginally more relative to the dry state under the CoM reference frame compared to the P-CoM reference frame.

Turning to Li^+ mobilities, we observe a significantly less pronounced increase in $\mu_{\mathrm{Li^+}}$ relative to the dry state under the CoM reference frame compared to P-CoM (cf. Figures S12B and 1C). However, the trends are still qualitatively consistent. Specifically, at low water content, $n_{\mathrm{Li^+{-}H_2O}} < 2$, $\mu_{\mathrm{Li^+}}$ is approximately constant relative to the dry state with an increase at higher water contents (cf. Figures S12D and 2B). This behavior corresponds to the crossover from all Li^+ ions being condensed with the polymer chains to a steady increase in the fraction of fast, “free” Li^+ ions (see the main paper and Section S2.2 for more details). As in the main paper, we also correlate the increase in μ_{Li^+} at high water content to an increase in the average water cluster size, where we observe a similar degree of correlation for the CoM and P-CoM reference frames (cf. Figures S12E and 3D. See the main paper for more details). This emphasizes the importance of considering various reference frames when conducting such analyses.

For completeness, Figure S13 presents the (A) TFSI^- and (B) Li^+ mobilities measured relative to the system CoM reference frame analogously to the P-CoM reference frame data in Figures S3B and C, respectively.

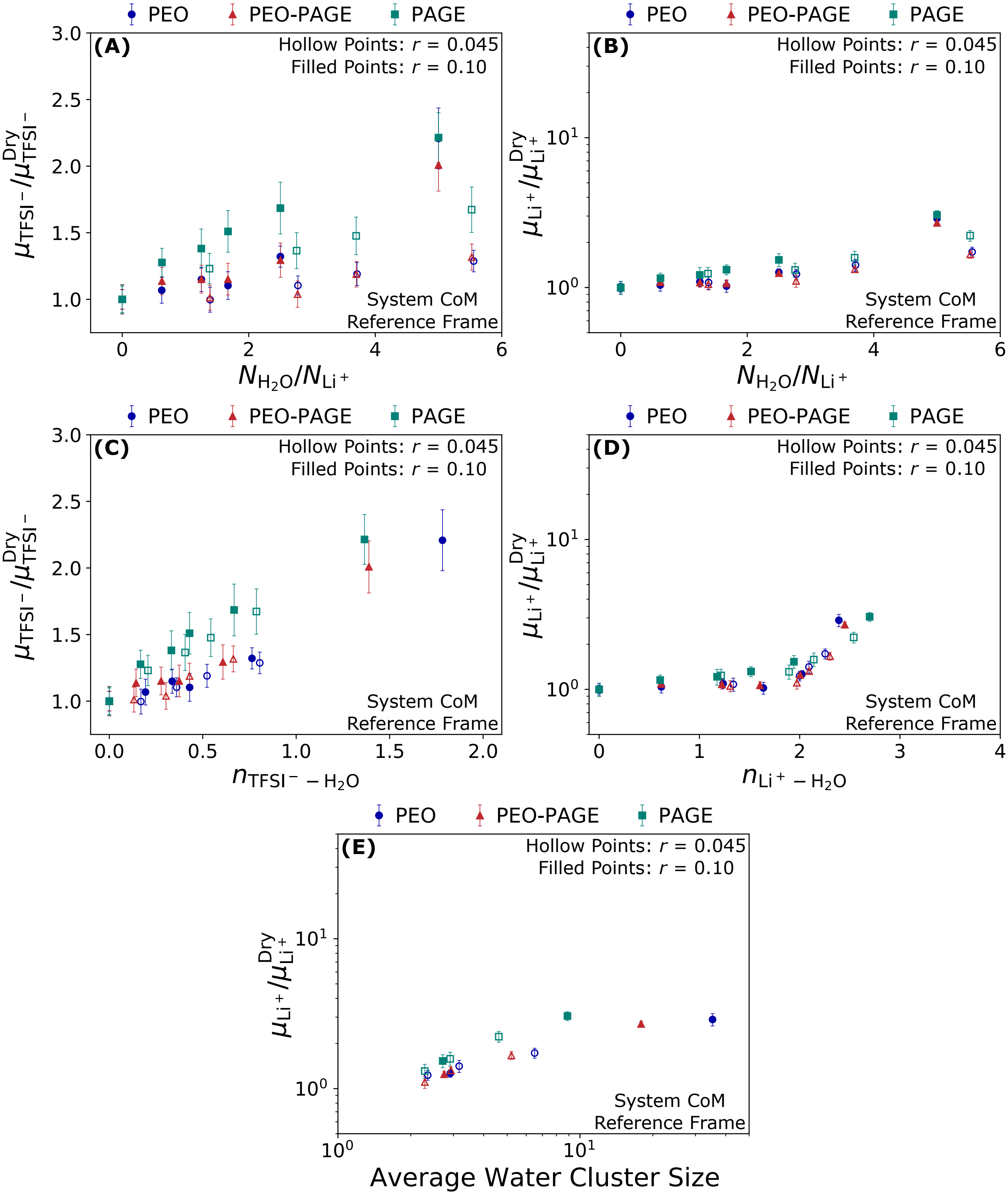

Figure S12: (A,C) $TFSI^-$ and (B,D,E) Li^+ mobilities relative to their values under dry conditions as a function of the (A,B) number of water molecules per Li^+ ion, (C,D) $i - H_2O$ solvation number, where i refers to the ion, and (E) average water cluster size, respectively. Hollow and filled points represent systems at lower ($r = 0.045$) and higher ($r = 0.10$) salt loadings, respectively. Mobilities are presented relative to the system center of mass reference frame.

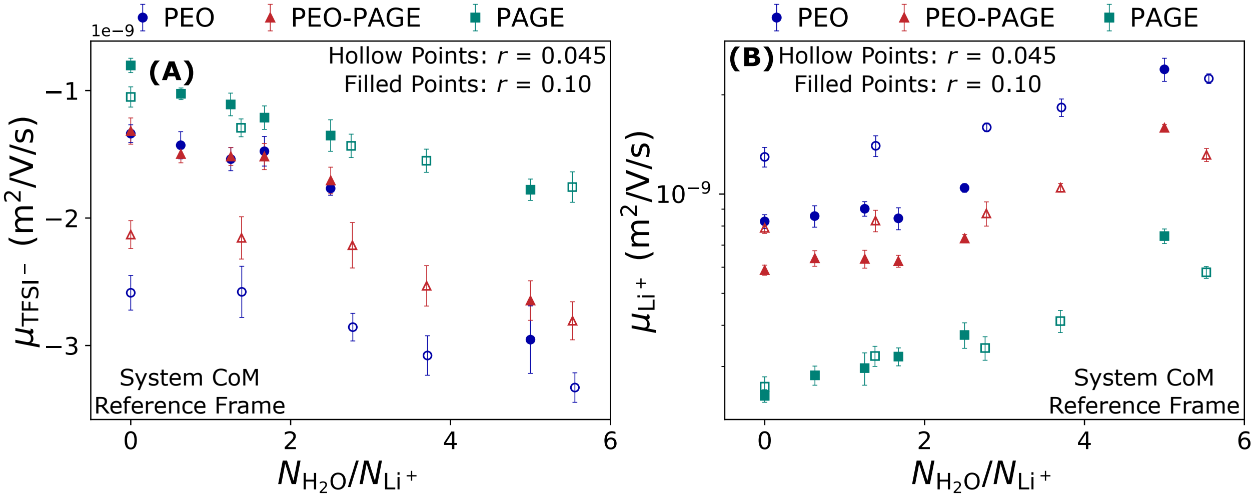

Figure S13: (A) TFSI$^-$ and (B) Li$^+$ mobilities as a function of the number of water molecules per Li$^+$ ion. Hollow and filled points represent systems at lower (r = 0.045) and higher (r = 0.10) salt loadings, respectively. Mobilities are presented relative to the system center of mass reference frame.

S3.2 Center of Volume Reference Frame

The CoV reference frame is calculated relative to the van der Waals volume of all atoms simulated within the system, where the van der Waals radii are taken from work by Bondi et al.[S30] Figure S14 presents the normalized (A,C) TFSI$^-$ and (B,D,E) Li$^+$ mobilities measured relative to the system CoV reference frame analogously to the P-CoM reference frame data in Figures 1B,C, 2A,B, and 3D (corresponding to Figures S14A-E, respectively). For ease of comparison, all data is plotted using the same scale as the main paper.

As in Section S3.1, we generally observe consistent trends between the CoV and P-CoM frames of reference. In comparing the CoM and CoV reference frames, we observe only minor differences between the two methods (cf. Figures S14 and S12). Therefore, the discussion above comparing CoM and P-CoM is broadly relevant for comparing CoV and P-CoM. Specifically, see the discussion on Figures S12A-E in Section S3.1 corresponding to Figures S14A-E in this section.

For completeness, Figure S15 presents the (A) TFSI$^-$ and (B) Li$^+$ mobilities measured relative to the system CoV reference frame analogously to the P-CoM reference frame data in Figures S3B and C, respectively.

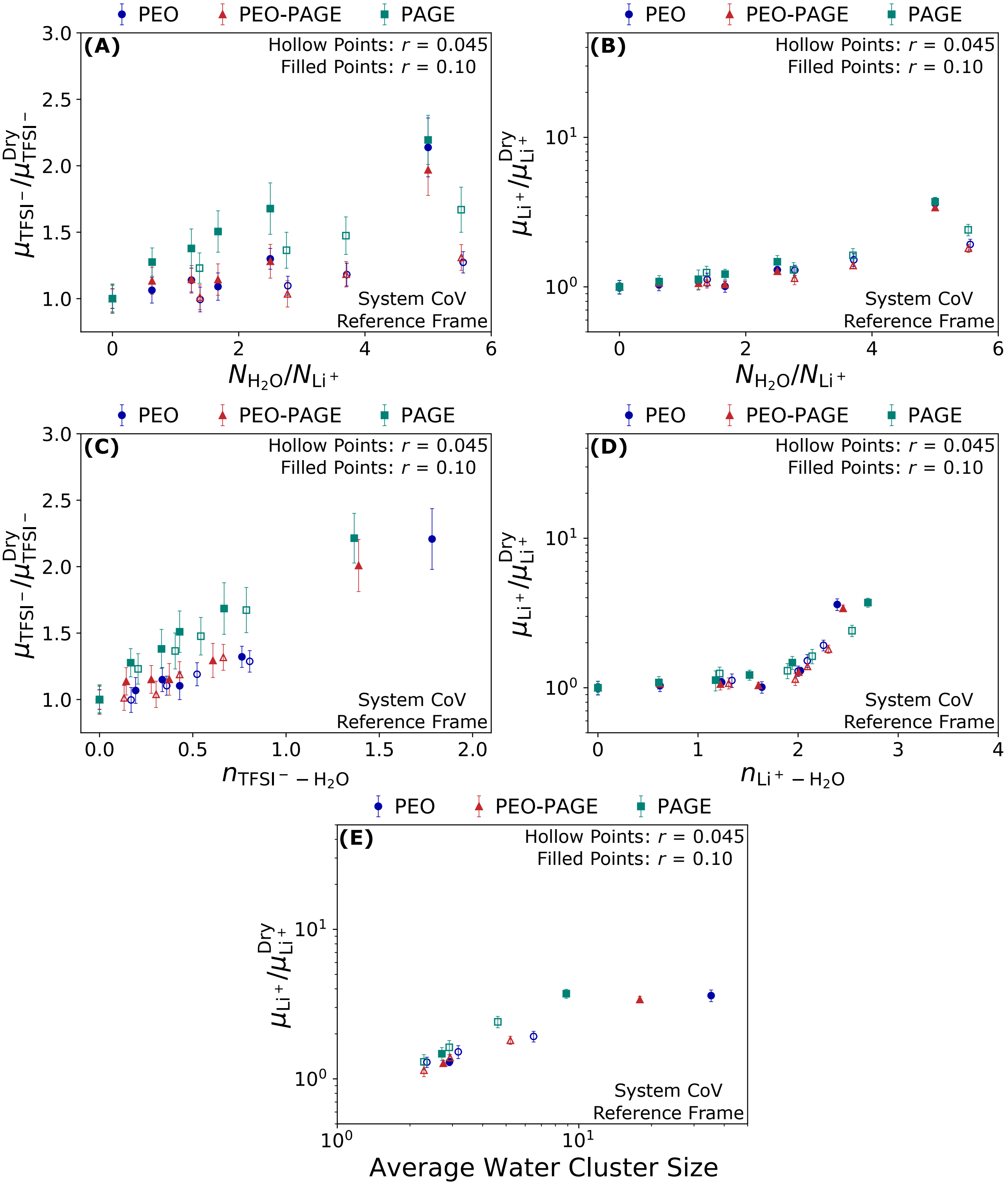

Figure S14: (A,C) $TFSI^-$ and (B,D,E) Li^+ mobilities relative to their values under dry conditions as a function of the (A,B) number of water molecules per Li^+ ion, (C,D) $i - H_2O$ solvation number, where i refers to the ion, and (E) average water cluster size, respectively. Hollow and filled points represent systems at lower ($r = 0.045$) and higher ($r = 0.10$) salt loadings, respectively. Mobilities are presented relative to the system center of mass reference frame.

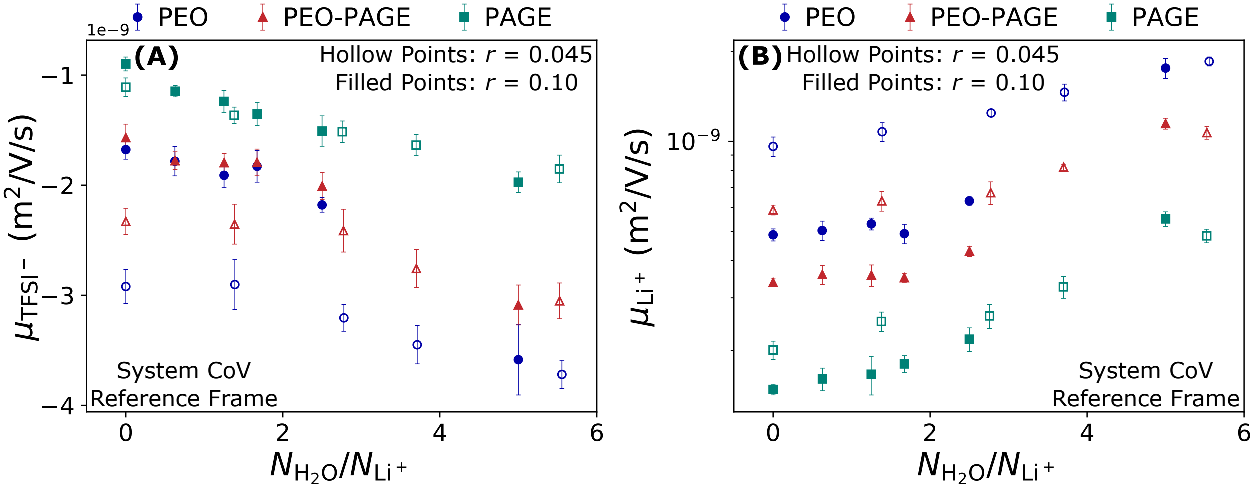

Figure S15: (A) $TFSI^-$ and (B) Li^+ mobilities as a function of the number of water molecules per Li^+ ion. Hollow and filled points represent systems at lower ($r = 0.045$) and higher ($r = 0.10$) salt loadings, respectively. Mobilities are presented relative to the system center of mass reference frame.

References

(S1) Abraham, M. J.; Murtola, T.; Schulz, R.; Páll, S.; Smith, J. C.; Hess, B.; Lindahl, E. GROMACS: High performance molecular simulations through multi-level parallelism from laptops to supercomputers. *SoftwareX* **2015**, *1*, 19–25.

(S2) Lindahl, E.; Abraham, M. J.; Hess, B.; Lindahl; van der Spoel, D. GROMACS 2020.5 Source code. 2021; `https://doi.org/10.5281/zenodo.4420785`.

(S3) Jorgensen, W. L.; Maxwell, D. S.; Tirado-Rives, J. Development and testing of the OPLS all-atom force field on conformational energetics and properties of organic liquids. *J. Am. Chem. Soc.* **1996**, *118*, 11225–11236.

(S4) Jorgensen, W. L.; Tirado-Rives, J. Potential energy functions for atomic-level simulations of water and organic and biomolecular systems. *Proc. Natl. Acad. Sci. U.S.A.* **2005**, *102*, 6665–6670.

(S5) Zeron, I.; Abascal, J.; Vega, C. A force field of Li^+, Na^+, K^+, Mg^{2+}, Ca^{2+}, Cl^-, and SO_4^{2-} in aqueous solution based on the TIP4P/2005 water model and scaled charges for the ions. *J. Chem. Phys.* **2019**, *151*, 134504.

(S6) Sambasivarao, S. V.; Acevedo, O. Development of OPLS-AA force field parameters for 68 unique ionic liquids. *J. Chem. Theory Comput.* **2009**, *5*, 1038–1050.

(S7) Doherty, B.; Zhong, X.; Gathiaka, S.; Li, B.; Acevedo, O. Revisiting OPLS force field parameters for ionic liquid simulations. *J. Chem. Theory Comput.* **2017**, *13*, 6131–6145.

(S8) Abascal, J. L.; Vega, C. A general purpose model for the condensed phases of water: TIP4P/2005. *J. Chem. Phys.* **2005**, *123*, 234505.

(S9) Lindahl, E.; Abraham, M. J.; Hess, B.; Lindahl; van der Spoel, D. GROMACS 2020.5 Manual. 2021; `https://doi.org/10.5281/zenodo.4420784`.

(S10) Lorentz, H. A. On the application of the virial theorem in the kinetic theory of gases. *Ann. Phys. (NY)* **1881**, *248*, 127–136.

(S11) Hockney, R. W.; Goel, S.; Eastwood, J. Quiet high-resolution computer models of a plasma. *J. Comput. Phys.* **1974**, *14*, 148–158.

(S12) Darden, T.; York, D.; Pedersen, L. Particle mesh Ewald: An $N\log(N)$ method for Ewald sums in large systems. *J. Chem. Phys.* **1993**, *98*, 10089–10092.

(S13) Essmann, U.; Perera, L.; Berkowitz, M. L.; Darden, T.; Lee, H.; Pedersen, L. G. A smooth particle mesh Ewald method. *J. Chem. Phys.* **1995**, *103*, 8577–8593.

(S14) Hess, B.; Bekker, H.; Berendsen, H. J.; Fraaije, J. G. LINCS: a linear constraint solver for molecular simulations. *J. Comput. Chem.* **1997**, *18*, 1463–1472.

(S15) Abbott, L. J.; Frischknecht, A. L. Nanoscale structure and morphology of sulfonated polyphenylenes via atomistic simulations. *Macromolecules* **2017**, *50*, 1184–1192.

(S16) Berendsen, H. J.; Postma, J. v.; Van Gunsteren, W. F.; DiNola, A.; Haak, J. R. Molecular dynamics with coupling to an external bath. *J. Chem. Phys.* **1984**, *81*, 3684–3690.

(S17) Bussi, G.; Donadio, D.; Parrinello, M. Canonical sampling through velocity rescaling. *J. Chem. Phys.* **2007**, *126*, 014101.

(S18) Parrinello, M.; Rahman, A. Polymorphic transitions in single crystals: A new molecular dynamics method. *J. Appl. Phys.* **1981**, *52*, 7182–7190.

(S19) Nosé, S.; Klein, M. Constant pressure molecular dynamics for molecular systems. *Mol. Phys.* **1983**, *50*, 1055–1076.

(S20) Zhang, Z.; Wheatle, B. K.; Krajniak, J.; Keith, J. R.; Ganesan, V. Ion Mobilities, Transference Numbers, and Inverse Haven Ratios of Polymeric Ionic Liquids. *ACS Macro Lett.* **2020**, *9*, 84–89.

(S21) Shen, K.-H.; Hall, L. M. Effects of ion size and dielectric constant on ion transport and transference number in polymer electrolytes. *Macromolecules* **2020**, *53*, 10086–10096.

(S22) Newman, J. S.; Thomas-Alyea, K. E. *Electrochemical systems*, 3rd ed.; Electrochemical Society series; Wiley: Hoboken, N.J, 2004.

(S23) Kann, Z.; Skinner, J. A scaled-ionic-charge simulation model that reproduces enhanced and suppressed water diffusion in aqueous salt solutions. *J. Chem. Phys.* **2014**, *141*, 104507.

(S24) Sujanani, R.; Nguyen, P. H.; Gordon, L. W.; Bamford, J. T.; Zele, A.; Pedretti, B. J.; Lynd, N. A.; Clément, R. J.; Segalman, R. A. Influence of Water Sorption on Ionic Conductivity in Polyether Electrolytes at Low Hydration. *ACS Macro Lett.* **2024**, *14*, 64–71.

(S25) Teran, A. A.; Tang, M. H.; Mullin, S. A.; Balsara, N. P. Effect of molecular weight on conductivity of polymer electrolytes. *Solid State Ion.* **2011**, *203*, 18–21.

(S26) Marioni, N.; Nordness, O.; Zhang, Z.; Sujanani, R.; Freeman, B. D.; Segalman, R. A.; Clément, R. J.; Ganesan, V. Ion and Water Dynamics in the Transition from Dry to Wet Conditions in Salt-Doped PEG. *ACS Macro Lett.* **2024**, *13*, 341–347.

(S27) Hansen, J.-P.; McDonald, I. R. I. R. *Theory of simple liquids with applications to soft matter*, 4th ed.; Academic Press: Oxford, England, 2013.

(S28) Lorenz, M.; Kilchert, F.; Nürnberg, P.; Schammer, M.; Latz, A.; Horstmann, B.; Schönhoff, M. Local volume conservation in concentrated electrolytes is governing charge transport in electric fields. *J. Phys. Chem. Lett.* **2022**, *13*, 8761–8767.

(S29) Harris, K. R.; Kanakubo, M. Effect of Relative Mass on Ion Velocity Cross-Correlations in Ionic Liquids and Molten Salts: Different Perspectives in Different Reference Frames. *J Phys. Chem. B* **2024**, *128*, 4504–4512.

(S30) Bondi, A. van der Waals volumes and radii. *J. Phys. Chem.* **1964**, *68*, 441–451.